Journal of Volcanology and Geothermal Research 328 (2016) 9–33

Contents lists available at ScienceDirect

Journal of Volcanology and Geothermal Research

journal homepage: www.elsevier.com/locate/jvolgeores

The eruptive history and magmatic evolution of Aluto volcano: new insights into silicic peralkaline volcanism in the Ethiopian rift

William Hutchison [a,*], David M. Pyle [a], Tamsin A. Mather [a], Gezahegn Yirgu [b], Juliet Biggs [c], Benjamin E. Cohen [d], Dan N. Barfod [d], Elias Lewi [e]

[a] COMET, Department of Earth Sciences, University of Oxford, South Parks Road, Oxford OX1 3AN, UK
[b] School of Earth Sciences, Addis Ababa University, P.O. Box 1176, Addis Ababa, Ethiopia
[c] COMET, School of Earth Sciences, University of Bristol, Wills Memorial Building, Queens Road, Bristol BS8 1RJ, UK
[d] NERC Argon Isotope Facility, Scottish Universities Environmental Research Centre, Rankine Avenue, East Kilbride, G75 0QF, UK
[e] IGSSA, Addis Ababa University, PO Box 1176, Addis Ababa, Ethiopia

ARTICLE INFO

Article history:
Received 6 July 2015
Received in revised form 30 August 2016
Accepted 19 September 2016
Available online 21 September 2016

Keywords:
silicic volcanism
eruptive history
peralkaline
volcanic hazard
geothermal resources
Main Ethiopian Rift

ABSTRACT

The silicic peralkaline volcanoes of the East African Rift are some of the least studied volcanoes on Earth. Here we bring together new constraints from fieldwork, remote sensing, geochronology and geochemistry to present the first detailed account of the eruptive history of Aluto, a restless silicic volcano located in a densely populated section of the Main Ethiopian Rift. Prior to the growth of the Aluto volcanic complex (before 500 ka) the region was characterized by a significant period of fault development and mafic fissure eruptions. The earliest volcanism at Aluto built up a trachytic complex over 8 km in diameter. Aluto then underwent large-volume ignimbrite eruptions at 316 ± 19 ka and 306 ± 12 ka developing a ~ 42 km^2 collapse structure. After a hiatus of ~250 ka, a phase of post-caldera volcanism initiated at 55 ± 19 ka and the most recent eruption of Aluto has a radiocarbon age of 0.40 ± 0.05 cal. ka BP. During this post-caldera phase highly-evolved peralkaline rhyolite lavas, ignimbrites and pumice fall deposits have erupted from vents across the complex. Geochemical modelling is consistent with rhyolite genesis from protracted fractionation (>80%) of basalt that is compositionally similar to rift-related basalts found east of the complex. Based on the style and volume of recent eruptions we suggest that silicic eruptions occur at an average rate of 1 per 1000 years, and that future eruptions of Aluto will involve explosive emplacement of localised pumice cones and effusive obsidian coulees of volumes in the range 1–100 × 10^6 m^3.

1. Introduction

Quaternary volcanism in the Ethiopian Rift has been marked by the eruption of hundreds of cubic kilometres of highly evolved silicic magmas (e.g., Mohr, 1971; Di Paola, 1972; Barberi et al., 1975; Lahitte et al., 2003; Peccerillo et al., 2003, 2007; Field et al., 2013). Silicic volcanoes have produced extensive rhyolitic lavas as well as pyroclastic density current (PDC) and tephra fall deposits; many show evidence of large (>10 km^3), geologically young (<500 ka), caldera-forming eruptions (e.g., Shala, Mohr et al., 1980; Gedemsa, Peccerillo et al., 2003 and Kone, Rampey et al., 2010, 2014) and several show signs of unrest (e.g., Corbetti, Aluto, Bora and Haledebi; Biggs et al., 2011; Hutchison et al., 2016). Many of these volcanoes are located in densely populated regions (Fig. 1A), and it is estimated that over 10 million people in Ethiopia live within 30 km of a Holocene volcanic centre (Brown et al., 2015). Our understanding of the eruptive histories of the silicic complexes is poor and hence there are large uncertainties as to the volcanic hazards they may pose in the future (Aspinall et al., 2011).

The focus of this study is the Aluto volcanic complex (Fig. 1B), a silicic peralkaline volcano which lies in the central sector of the Main Ethiopian Rift (MER), and for which few details of its eruptive past are known. Aluto is currently restless, having undergone episodic ground deformation for at least the past decade (Biggs et al., 2011; Hutchison et al., 2016). This is of particular concern given that several thousand people live on the volcano as well as in the nearby towns of Ziway, Adami Tullo and Bulbula (each with populations in the range of 10,000–50,000, Central Statistical Agency of Ethiopia, 2012), and according to the Smithsonian Global Volcanism Program (Siebert and Simkin, 2002), 6.8 million people live within 100 km of the volcano. Aluto also hosts Ethiopia's only geothermal power plant (e.g., Gizaw, 1993; Gianelli and Teklemariam, 1993; Teklemariam et al., 1996), and while the plant is only producing 7 MW at present there are plans for significant expansion. Locating this major infrastructure on a volcanic edifice where eruptive frequency is unknown poses inherent risks (e.g., Wilson et al., 2012, 2014).

* Corresponding author at: Department of Earth and Environmental Sciences, University of St. Andrews, KY16 9AL, UK.
E-mail address: wh39@st-andrews.ac.uk (W. Hutchison).

http://dx.doi.org/10.1016/j.jvolgeores.2016.09.010

Knowledge of Aluto's eruptive history is also of considerable importance for regional palaeoclimate and palaeoanthropological studies. Aluto lies in the centre of the Ziway-Shala lake basin (Fig. 1B), a key East African intracontinental rift basin that preserves palaeoclimate proxy records (e.g., Gasse and Street, 1978; Street, 1979; Le Turdu et al., 1999; Benvenuti et al., 2002, 2013; Gibert et al., 2002) as well as archaeological records of Middle and Later Stone Age (280–11 ka) hominin populations (e.g., Laury and Albritton, 1975; Morgan and Renne, 2008; Sahle et al., 2013, 2014; Ménard et al., 2014; Benito-Calvo et al., 2014). An understanding of volcanism in this basin is complementary to these studies, because edifice development will change the rates and spatial patterns of sediment accumulation which preserve palaeoclimate records (Le Turdu et al., 1999); widely dispersed tephra derived from these volcanoes form the key marker horizons that constrain the rates of hominin evolution and dispersal (e.g., Morgan and Renne, 2008; WoldeGabriel et al., 2005); and volcanoes have provided

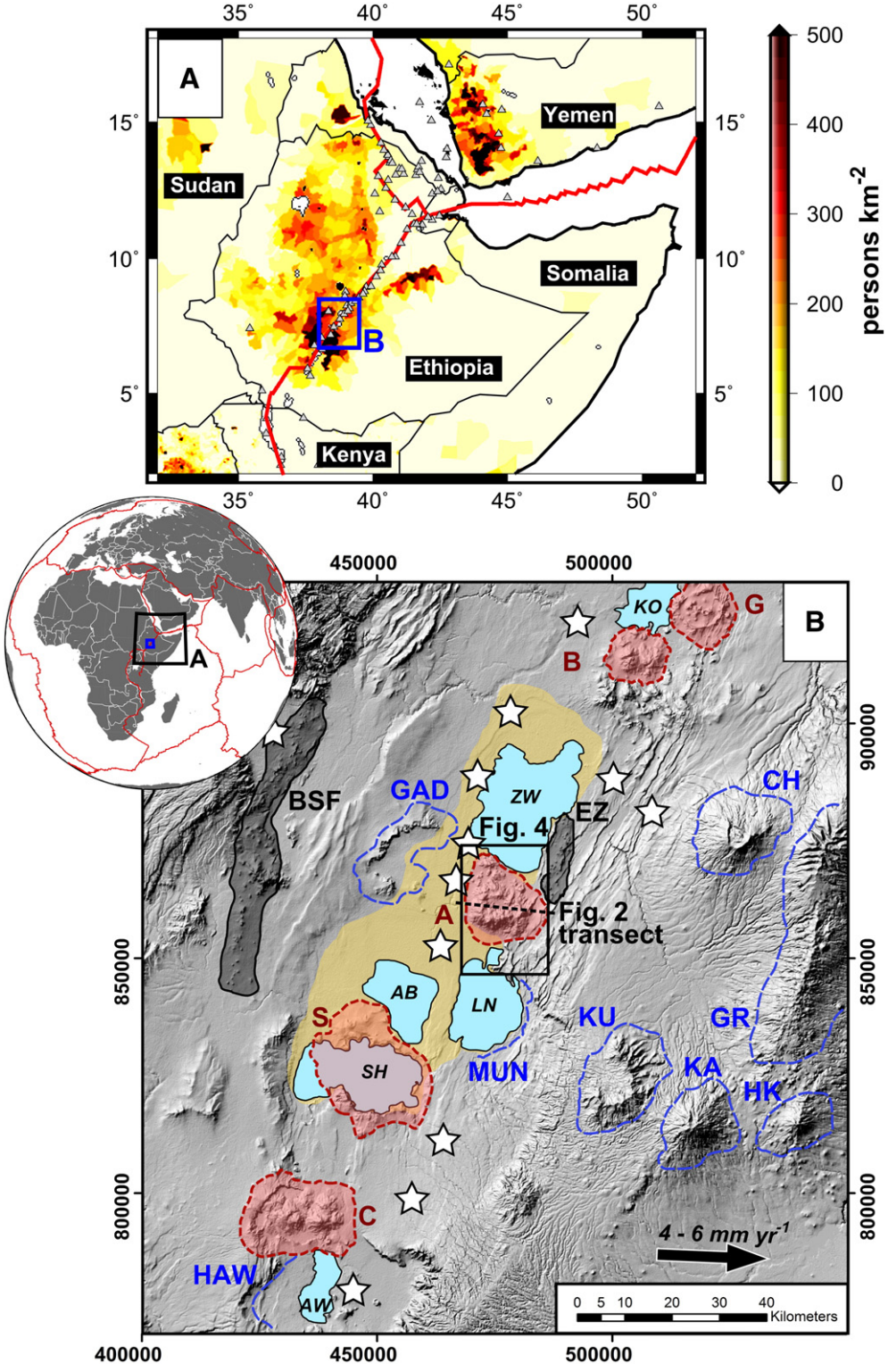

important resources (e.g., obsidian) that hominin populations have worked and transported since the earliest Palaeolithic, 1.7 million years ago (e.g., Piperno et al., 2009).

In this paper, field studies, remote sensing, geochronology and geochemical techniques are integrated to document the volcanic and magmatic evolution of the Aluto volcanic complex. We reconstruct the eruptive history of Aluto and present a new geological map (Section 5); we present the first dedicated whole-rock geochemical study of the volcano, and assess magma petrogenesis (Section 6), and finally, we develop a conceptual model of the eruptive history and magmatic evolution of the complex within the context of the evolving rift (Section 7).

2. Regional Tectonic and Volcanic Overview

The MER is an active continental rift that forms the northernmost section of the East African Rift System (see reviews by Ebinger, 2005; Corti, 2009). It is a classic example of an oblique rift (Corti et al., 2013) and is traditionally sub-divided into northern, central and southern segments that reflect prominent spatial variations in fault architecture and lithospheric characteristics (e.g., Hayward and Ebinger, 1996; Bonini et al., 2005; Keranen and Klemperer, 2008; Agostini et al., 2011). Aluto lies in the central MER (CMER) where the pattern of faulting is characterized by two distinct groups: (1) boundary faults located on the margins of the rift, and (2) localized internal faults, mapped as 'Wonji' faults (Agostini et al., 2011; Keir et al., 2015). The boundary faults formed during the initial stages of rifting (at 8–6 Ma in the CMER, WoldeGabriel et al., 1990; Bonini et al., 2005) and appear to facilitate very limited tectonic extension at present (Keir et al., 2006; Pizzi et al., 2006; Agostini et al., 2011). The Wonji faults, located in the ~15 km wide axial zone of the rift, are short, right-stepping en-echelon features that developed after ~2 Ma (Boccaletti et al., 1998; Ebinger and Casey, 2001) and are the focus of present-day tectonic strain (Keir et al., 2006, 2015; Agostini et al., 2011).

There has been surface volcanism throughout the development of the MER (WoldeGabriel et al., 1990, 1992, 2000; Abebe et al., 2007) but full understanding of the links between volcanic evolution and rift development is still hampered by a lack of detailed eruption chronologies for many individual volcanoes (Corti, 2009). Prior to development of the silicic volcanoes exposed along the rift axis today (including: Gedemsa, Bora-Berrecio, Aluto, Shala and Corbetti, Fig. 1B), several large silicic caldera-forming volcanoes were active in the MER during the Early Pliocene–Early Pleistocene (4–1 Ma, Fig. 1B). Tuff deposits from these volcanoes are often found in fault sections on the margins of the rift (e.g., WoldeGabriel et al., 1990, 1992), while the associated caldera structures are deeply eroded or otherwise completely covered by younger basin-filling sediments (WoldeGabriel et al., 1990; Le Turdu et al., 1999). Three of the largest silicic caldera-forming volcanoes (Munesa, Awassa and Gademotta) formed within the axial region of the CMER (Fig. 1B), and are now extinct. At Munesa caldera climactic eruptions are dated at ~3.5 Ma (WoldeGabriel et al., 1990, 1992; Le Turdu et al., 1999), at Awassa caldera major eruptions took place at 1.85–1.1 Ma (WoldeGabriel et al., 1990) and at Gademotta (~20 km NW of Aluto) the final phase of activity is dated to ~1.3 Ma (Vogel et al., 2006). Volcanism in the MER, prior to 1 Ma, was diffuse and encompassed a wide footprint of the rift zone (Bonini et al., 2005; Corti, 2009; Maccaferri et al., 2014), as evidenced by off-axis trachytic and basaltic volcanic centres (e.g., Chilalo, Hunkuolo, Kaka, Kubsa, Fig. 1B; Mohr and Potter, 1976; WoldeGabriel et al., 1990).

Since 0.65 Ma, eruptive activity has been focused within right-stepping, en-echelon volcanic segments along the axis of the rift that are co-located with the zones of Wonji faulting (Abebe et al., 2007; Corti, 2009; Beutel et al., 2010; Keir et al., 2006, 2015). Volcanism has been strongly bimodal (Abebe et al., 2007). Mafic rocks form cinder cone fields and lava flow deposits that are often aligned along Wonji fault networks (e.g., East Ziway, Fig. 1B, Abebe et al., 2007; Rooney et al., 2007). Silicic rocks are peralkaline and represented by large complexes 10–20 km in diameter located along the axis of the rift (Di Paola, 1972). The silicic volcanoes have compositionally zoned magma chambers (Peccerillo et al., 2003, 2007; Ronga et al., 2009), and the majority have undergone large-volume ignimbrite eruptions (>> 1 km^3), creating calderas that scar the present day rift zone (e.g., Acocella et al., 2002; Rampey et al., 2010). In the waning stages of silicic magmatic activity basaltic lavas have erupted directly through the floor of the calderas (e.g., at Gedemsa: Peccerillo et al., 2003 and Kone: Rampey et al., 2010).

There are limited accounts of historical volcanic activity in the MER and the only reported eruptions occurred at Fantale and Kone volcanoes in the 1800–1830's (Williams et al., 2004; Rampey et al., 2010). While satellite remote sensing has detected ground deformation at various silicic complexes, including Aluto (Biggs et al., 2011; Hutchison et al., 2016), it is important to underscore that not one of the MER volcanoes is routinely monitored on the ground (Aspinall et al., 2011). Therefore, at present, to assess the likelihood of future eruptions in the MER, volcanologists must rely on remote sensing to detect magma movement in the subsurface, as well as geochronology to constrain the rates of past eruptive activity.

3. Previous Studies of Aluto

The earliest geological descriptions of Aluto come from regional scale mapping reports (e.g., Dakin and Gibson, 1971; Di Paola, 1972). These studies identified that the bulk of recent volcanic products of Aluto are rhyolitic PDC deposits and obsidian coulees. Di Paola (1972) recognized that various craters and lava flow deposits exist along predominantly NNE-SSW orientations, parallel to the Wonji fault structures, while Dakin and Gibson (1971) postulated that there had been a caldera-forming event at Aluto based on field evidence for a ~ 1 km long segment of the caldera wall visible on the north-east of the complex.

In 1970 the Aluto-Langano region was identified as a site for geothermal development and eight exploratory wells were completed between 1981 and 1985 (ELC Electroconsult, 1986). Geological mapping was undertaken at the same time (Kebede et al., 1985), and lithological descriptions were also completed for deep wells LA-4 and LA-8, see Tables S1 and S2, respectively (Yimer, 1984; Mamo, 1985). Using the cores and cuttings collected during deep well drilling, several previous publications (e.g., Gizaw, 1993; Gianelli and Teklemariam, 1993; Teklemariam et al., 1996), and drilling reports (Yimer, 1984; Mamo, 1985; ELC Electroconsult, 1986; Teklemariam, 1996), have established a deep stratigraphy of the complex. In Fig. 2 we summarize the Aluto

Fig. 1. A) Map of Ethiopia and neighbouring countries overlain with population density. Red lines indicate major plate boundaries and grey triangles show Quaternary volcanic centres (after Siebert and Simkin, 2002). Population data are estimates for 2015 provided by Socioeconomic Data and Applications Center (SEDAC), http://sedac.ciesin.columbia.edu. Population values are extrapolated based on a combination of national growth rates from United Nations statistics and sub-national growth rates from census dates. The blue rectangle marked B, shows the area covered by the Digital Elevation Model (DEM) in Fig. 1B. **B)** Hillshade Satellite Radar Topography Mission DEM showing the location of the Aluto volcanic complex (marked A) within the central segment of the Main Ethiopian Rift (MER). Quaternary silicic volcanic complexes are shaded red, and include: Corbetti (marked C), Shala or O'a caldera (marked S); Bora-Bericcio (marked B) and Gedemsa (marked G). Recent mafic cinder cones and lavas of East Ziway (marked EZ) and the Butajira-Silti field (marked BSF) are shown by the dark grey shaded areas. Silicic volcanic complexes that became extinct prior to 1 Ma are outlined by the blue dashed lines, and include: Hawasa (marked HAW), Munesa (marked MUN), Gademotta (marked GAD), Kubsa (marked KU), Kaka (marked KA), Chilalo (marked CH), Hunkuolo (marked HK) and the Galama Range (marked GR). The beige shaded area identifies the maximum extent of the Ziway-Shala lake basin that developed in the Mid–Late Pleistocene (Le Turdu et al., 1999; Benvenuti et al., 2002, 2013). The major present-day lakes are identified as: Ko: Lake Koka; Zw: Lake Ziway; Ln: Lake Langano; Ab: Lake Abijta, Sh: Lake Shala and AW: Lake Awasa. White stars identify centres of population with >10,000 inhabitants. Current extension of the MER, after Keir et al. (2006), Bendick et al. (2006) and Saria et al. (2014), is indicated by the black arrow with motion relative to a fixed Nubian plate. The black and blue outlined areas on the globe inset correspond to the regions covered in Fig. 1A and B, respectively.

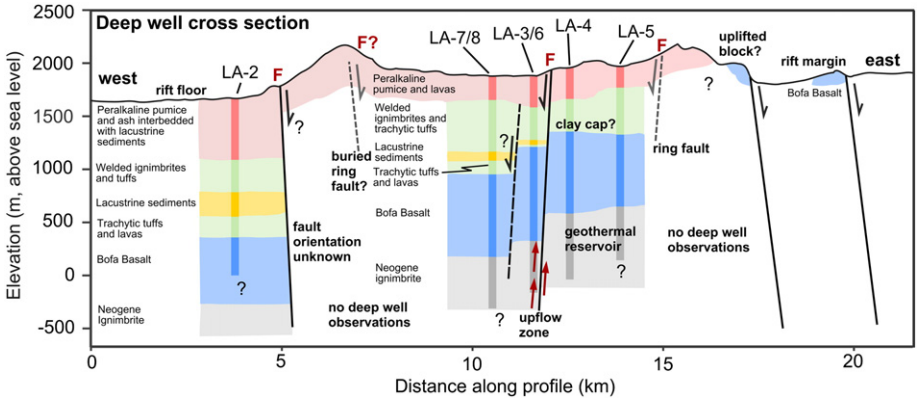

Fig. 2. West-east cross section showing the deep stratigraphy and hypothesized subsurface structures on Aluto (after Hutchison et al., 2015). Note that the transect line is shown in Fig. 1B. Well data represent the synthesis of several publications (Gizaw, 1993; Gianelli and Teklemariam, 1993; Teklemariam et al., 1996) and drilling reports provided by the Geological Survey of Ethiopia (Yimer, 1984; Mamo, 1985; ELC Electroconsult, 1986; Teklemariam, 1996). The geological units shown have been correlated between the different wells on Aluto (Gizaw, 1993; Gianelli and Teklemariam, 1993) and indicate a prevailing mode of deposition rather than a single homogeneous unit (e.g., paleosols occur within the Bofa Basalt, see Section 5.1 for detailed descriptions). Red arrows indicate main upflow zone of geothermal reservoir along the Artu Jawe fault zone (Gianelli and Teklemariam, 1993; Teklemariam et al., 1996; Hutchison et al., 2015, 2016). Red 'F' labels indicate major fumarole and degassing regions mapped at the surface of the volcano (after Hutchison et al., 2015).

deep well stratigraphy and also overlay major structural features recognized by Hutchison et al. (2015). Lithological descriptions of the units are provided in Section 5.1 and Fig. 3.

The only previous interpretations of the eruptive history of Aluto were made by Kebede et al. (1985) and ELC Electroconsult (1986). They each proposed a period of sub-aerial basaltic eruptions (Bofa Basalts, at 1.6 ± 0.5 Ma, Table 1) prior to the first silicic volcanism. Silicic eruptions at Aluto then built up an early dome complex, culminating in several large ignimbrite eruptions and caldera collapse. K/Ar dates (cited in Teklemariam et al., 1996) suggested that the climactic phases of eruption took place at ~155 ka (Table 1). Subsequent investigations of Aluto have focussed on the geothermal field (e.g., Gebregzabher,

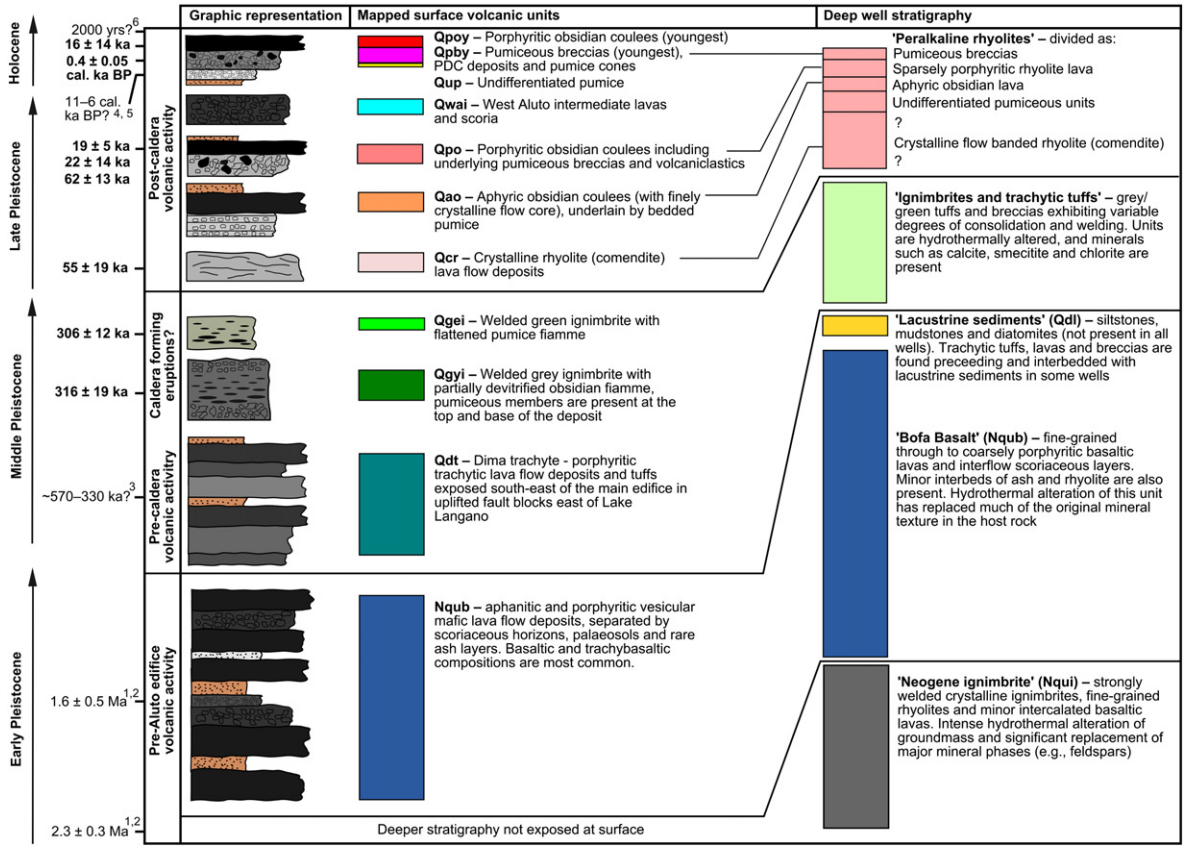

Fig. 3. Stratigraphic summary correlating the volcanic units mapped at the surface (Fig. 4) with the lithological sequence reconstructed from deep well cores and cuttings (Yimer, 1984; Mamo, 1985; ELC Electroconsult, 1986; Gizaw, 1993; Gianelli and Teklemariam, 1993; Teklemariam, 1996; Teklemariam et al., 1996). Colours of the mapped surface volcanic units correspond with the shading in the geological map in Fig. 4. The relative thickness of each unit corresponds to the height of the coloured rectangle. Ages marked to the left of the stratigraphy are from our new $^{40}Ar/^{39}Ar$ determinations or radiocarbon ages unless indicated otherwise by numerical superscripts. Literature ages are from: [1]: Teklemariam, 1996; [2]: Teklemariam et al., 1996; [3]: Le Turdu et al., 1999; [4]: Gasse and Street, 1978; [5]: Benvenuti et al., 2013; [6]: Gianelli and Teklemariam, 1993.

Table 1
Compilation of new and existing age constraints on volcanism at Aluto. $^{40}Ar/^{39}Ar$ ages shown are the weighted mean ± standard error of the mean (1σ), and in brackets the arithmetic mean ± one standard deviation (we quote the latter throughout the manuscript). Errors on other ages are quoted as originally published. Radiocarbon dates were calibrated with IntCal13 (Reimer et al., 2013) and OxCal v.4.2. Calibrated radiocarbon ages (2σ confidence interval) represent the age range of the deposits below and above the tephra layer, respectively.

	Sample location							
Sample	Lat (°N)	Lon (°E)	Rock type	Unit	Method	Age	Reference	Additional notes
18 11 07a	7.69173	38.79719	ignimbrite	Qgyi	$^{40}Ar/^{39}Ar$ (sanidine)	316 ± 12 (316 ± 19) ka	Hutchison et al. (in press)	
13 05 04	7.84068	38.73031	ignimbrite	Qgei	$^{40}Ar/^{39}Ar$ (sanidine)	306 ± 8 (306 ± 12) ka	Hutchison et al. (in press)	
18 02 04	7.74193	38.80486	comenditic rhyolite	Qcr	$^{40}Ar/^{39}Ar$ (sanidine)	55 ± 9 (55 ± 19) ka	Hutchison et al. (in press)	
18 01 08	7.83245	38.74576	obsidian	Qpo	$^{40}Ar/^{39}Ar$ (sanidine)	18 ± 10 (22 ± 14) ka	this study	
30 01 LNE	7.81176	38.79360	obsidian	Qpo	$^{40}Ar/^{39}Ar$ (sanidine)	18 ± 8 (19 ± 5) ka	Hutchison et al. (in press)	
01 02 14	7.77725	38.76988	obsidian	Qpo	$^{40}Ar/^{39}Ar$ (sanidine)	61 ± 8 (62 ± 13) ka	this study	
31 01 LE	7.78321	38.82680	obsidian	Qpoy	$^{40}Ar/^{39}Ar$ (sanidine)	12 ± 7 (16 ± 14) ka	Hutchison et al. (in press)	
31–01-08	7.79333	38.81778	tephra	Qpby	^{14}C (charcoal)	0.40 ± 0.05 cal. ka BP	Hutchison et al. (in press)	beneath pumiceous pyroclastic deposits
unknown	unknown (south of Gademotta)		ignimbrite	unknown	K/Ar (phase unknown)	155 ± 8 ka	ELC Electroconsult (1986)	dating procedure and error on age not reported, ignimbrite apparently overlain by the lacustrine sediments
29 BT82	7.81667	38.75833	obsidian	Qpo?	K/Ar (groundmass)	42 ± 10 ka	WoldeGabriel et al. (1990)	
30 BT79A	7.74167	38.79167	rhyolite	Qao?	K/Ar (groundmass)	78 ± 20 ka	WoldeGabriel et al. (1990)	
31 LA3	7.79167	38.80000	ignimbrite	Nqui	K/Ar (feldspar)	1390 ± 100 ka	WoldeGabriel et al. (1990)	crystal rich welded tuff from deep well, pervasive hydrothermal alteration of sample
33 BT92	7.86667	38.90833	basalt	Nquw	K/Ar (groundmass)	290 ± 100 ka	WoldeGabriel et al. (1990)	hawaiite from east of Lake Ziway
S-1	rift escarpment near Munesa		ignimbrite	Nqui	K/Ar (sanidine)	2300 ± 300 ka	Teklemariam, 1996	
S-1	rift escarpment near Munesa		ignimbrite	Nqui	K/Ar (glass)	2300 ± 500 ka	Teklemariam (1996)	
S-2	eastern flank of Aluto		basalt	Nqub	K/Ar (plagioclase)	1600 ± 500 ka	Teklemariam (1996)	
Abernosa pumice (Deka Wede)	7.79249	38.68877	tephra	Qpo tephra?	^{14}C (lacustrine silt and charcoal)	26.41 ± 0.64 to 13.86 ± 0.43 cal. ka BP	Street (1979), Le Turdu et al. (1999), Benvenuti et al. (2002), Ménard et al. (2014)	thick volcaniclastic sequence with ~13 distinct tephra layers
Pumice lapilli (Deka Wede)	7.79249	38.68877	tephra	Qup?	^{14}C (lacustrine marl and charcoal)	12.26 ± 0.27 to 9.55 ± 0.28 cal. ka BP	Street (1979), Le Turdu et al. (1999), Benvenuti et al. (2002), Ménard et al. (2014)	pumice overlying fluvial sands, above the Abernosa pumice
Pumice (Deka Wede)	7.79249	38.68877	tephra	Qup?	^{14}C (charcoal and melanoides shells)	9.55 ± 0.28 to 6.60 ± 0.13 cal. ka BP	Street (1979), Le Turdu et al. (1999), Benvenuti et al. (2002), Ménard et al. (2014)	pumice overlying palaeosol, youngest tephra at Deka Wede
Pumice (Haroresa)	7.67408	38.81026	tephra	Qup?	^{14}C (melanoides shells)	11.12 ± 0.11 to 7.29 ± 0.06 cal. ka BP	Benvenuti et al. (2013)	pumice bracketed by gravels, youngest tephra at Haroresa

1986; Valori et al., 1992; Gizaw, 1993; Gianelli and Teklemariam, 1993; Teklemariam et al., 1996; Saibi et al., 2012) and the outline eruptive history proposed by Kebede et al. (1985) and ELC Electroconsult (1986) has not been re-evaluated within the last forty years.

4. Sampling and Analytical Techniques

Our stratigraphy was established from a total of 8 weeks of field mapping conducted during 2012–2014. Further, the Natural Environment Research Council's Airborne Research and Survey Facility (NERC-ARSF) acquired high-spatial resolution topography (lidar), hyperspectral data and aerial photographs of the complex on 16th November 2012. Digital geological mapping was carried out in ArcGIS and involved analysis of orthorectified aerial photos, the lidar DEM as well as Google Earth and ASTER satellite imagery for regions beyond coverage of the lidar DEM. Volcanic and tectonic fault structures were mapped by Hutchison et al. (2015) using remote sensing techniques and soil-CO_2 degassing surveys. The volumes of recent volcanic deposits (obsidian coulees and pumice cones) were estimated using the lidar DEM following the methods of Nomikou et al. (2014). In brief, we use polygons to outline and mask out the deposit from the DEM. After removing this region from the DEM we then interpolated a smoothed near-flat pre-eruption surface across the masked area (processing was carried out in GMT software using a variable tension parameter, Nomikou et al., 2014). We then subtracted the present-day DEM from the interpolated DEM to calculate the residual volume between the surfaces, thus providing a volume estimate for the volcanic deposit. An example of this technique is given in Fig. S1. At Santorini volcano, lava flow maximum and minimum volumes were calculated by Nomikou et al. (2014) and typically varied by <25%; we use this value as an estimate

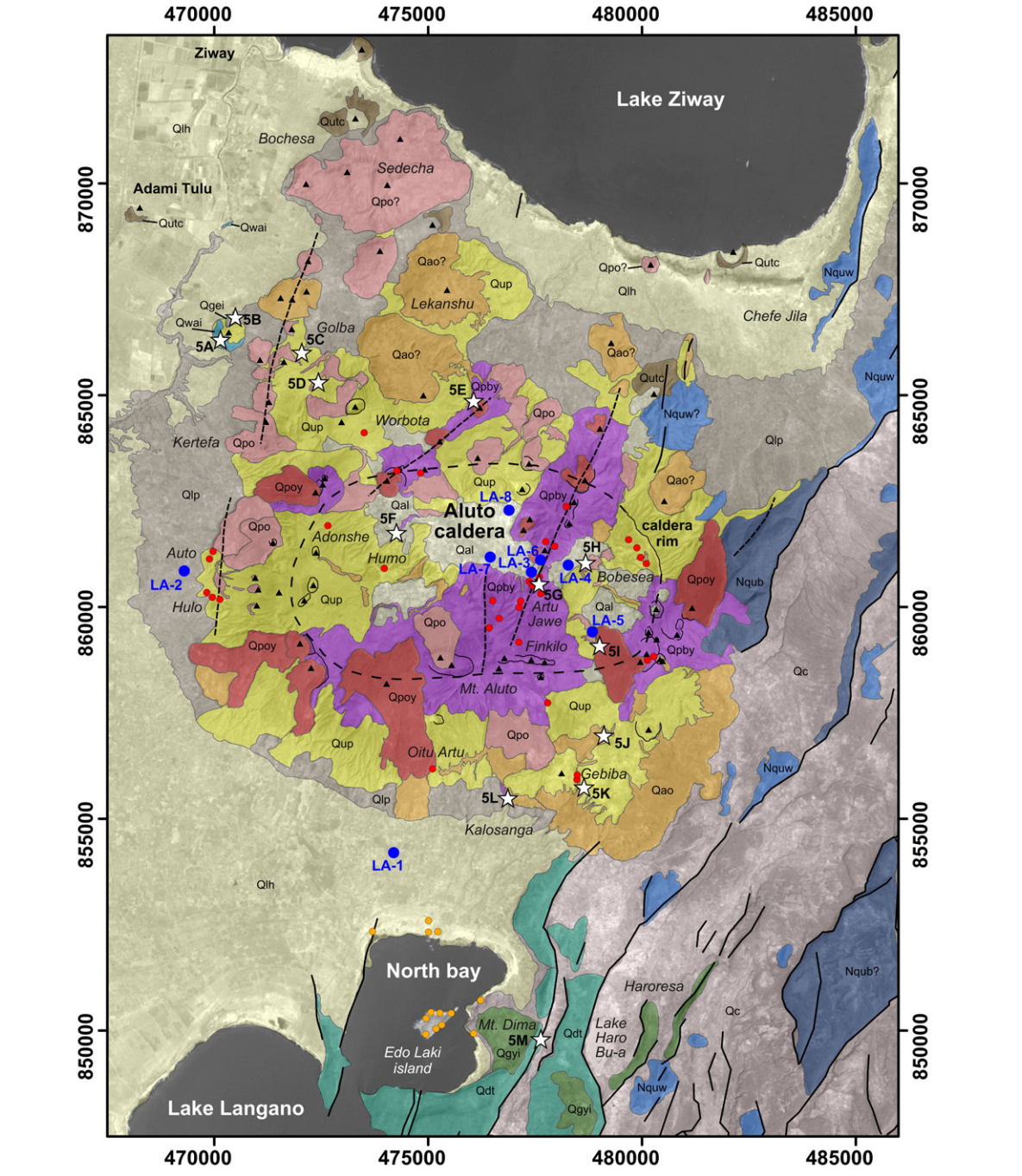

Peralklaine rhyolites (post-caldera)

- Qpoy: Porphyritic obsidian coulees (youngest)
- Qpby: Pumiceous breccias, PDCs and pumice cones (youngest)
- Qup: Undifferentiated pumice
- Qwai: West Aluto intermediate lavas and scoria cones
- Qpo: Porphyritic obsidian coulees
- Qao: Aphyric obsidian coulees (including underlying bedded pumice)
- Qcr: Comenditic rhyolite

Welded ignimbrites (caldera-forming eruptions?)

- Qgei: Welded green ignimbrite
- Qgyi: Welded grey ignimbrites and associated pyroclastics

Trachytes (pre-caldera?)

- Qdt: Trachytic tuffs and lavas

Pre-Aluto mafic activity

- Nqub: Undifferentiated mafic lavas

Undifferentiated volcanics

- Nquw: Undifferentiated Wonji scoria cones
- Qutc: Undifferentiated tuff cone

Sedimentary rocks

- Qal: Alluvium and reworked volcaniclastics
- Qlh: Holocene lacustrine sediments
- Qlp: Pleistocene lacustrine sediments
- Qc: Colluvial and fluvial deposits (gravels, sands and muds)

Symbols

- Fault
- Crater
- Fault (inferred)
- Volcanic vent
- Fumarole vents
- Hot springs
- Deep geothermal well
- Stratigraphic section (Fig. 5)

of the volume uncertainty of this method. Finally, as the internal structure of the silicic domes on Aluto is poorly constrained we simply present the total volume of the deposit rather than a dense rock equivalent.

We obtained $^{40}Ar/^{39}Ar$ age determinations at key points in the stratigraphic sequence (Fig. 3). Unweathered lava and bulk ignimbrite samples were collected in the field and pulverised in a jaw-crusher. Sanidine phenocrysts (250–500 μm in diameter) were separated from the crush using magnetic as well as lithium metatungstate heavy liquid density separation techniques. The phenocrysts were then leached ultrasonically in 5% HF for ~3 min to remove adhering glass and groundmass. Grains were rinsed in distilled water and dried, followed by handpicking under a binocular microscope to remove any remaining contaminant phases (e.g., fluid/melt inclusions, quartz or granophyric textured crystals). Samples were irradiated in the Cd-lined facility at the Triga Reactor, Oregon State University, and subsequently analysed at the Natural Environment Research Council (NERC) Argon Isotope Facility, Scottish Universities Environmental Research Centre (SUERC). Five $^{40}Ar/^{39}Ar$ ages and one radiocarbon age determined for Aluto were reported by Hutchison et al. (in press), who used these ages to examine silicic magma fluxes in the MER. In this study we use these existing ages, plus an additional two $^{40}Ar/^{39}Ar$ ages, to examine stratigraphic relationships and the rates of recent volcanism at Aluto. A limited number of geochronological data have been presented previously for Aluto; these are shown alongside our new $^{40}Ar/^{39}Ar$ ages in Table 1.

A total of 36 lava and pumice samples were selected for whole-rock chemical analysis. Samples were trimmed of weathered material, and powdered in an agate ball mill. Major and selected trace element analysis was conducted at the Department of Geology at the University of Leicester by X-ray fluorescence (XRF) using a PANalytical Axios-Advanced XRF spectrometer (glass fusion beads were prepared for major elements, and powder pellets were prepared for trace elements). A complete suite of trace elements were also analysed by Inductively Coupled Plasma-Mass Spectroscopy (ICP-MS) at the Department of Earth Sciences, University of Oxford. For this, solutions of powdered samples were produced in a multi-stage method, involving initial hot, low-pressure digestion in HF and HNO_3, followed by multiple drying and dissolution steps using HNO_3, before final dilution in HNO_3. Standard analyses for both XRF and ICP-MS methods were within 10% of their reference values. This project has also compiled previously published element data for the Aluto volcanic complex (from Di Paola, 1972; Yimer, 1984; Mamo, 1985; Teklemariam, 1996). Both previous and new bulk major and trace element data, a total of 45 samples, are presented in Table S3a–d.

5. Volcanic Stratigraphy

We have divided the stratigraphic relations as follows: Section 5.1 presents the deep well stratigraphy compiled from previous publications; Section 5.2 presents our field stratigraphy from surface mapping, and Section 5.3 presents age constraints and correlations between the surface and subsurface stratigraphy.

5.1. Deep well stratigraphy

Previous publications on the geothermal field of Aluto (Gizaw, 1993; Gianelli and Teklemariam, 1993; Teklemariam et al., 1996) and drilling reports provided by the Geological Survey of Ethiopia (Yimer, 1984; Mamo, 1985; ELC Electroconsult, 1986; Teklemariam, 1996) have been used to establish a composite deep stratigraphy for Aluto (Fig. 3, right-hand column). In the following sections the unit name of previous authors is shown first, followed by our revised classification in brackets (justified in Section 5.3).

5.1.1. Neogene Ignimbrites (Neogene-Quaternary undifferentiated ignimbrites, Nqui)

The base of all deep wells is represented by a sequence of rhyolitic ignimbrites and lavas at least 400–500 m thick (Gizaw, 1993; Gianelli and Teklemariam, 1993; Teklemariam et al., 1996; Figs. 2, 3). Welded crystal-rich ignimbrites and fine-grained rhyolites dominate the sequence but volumetrically subordinate basaltic lava layers are also observed (Yimer, 1984; Mamo, 1985). The ignimbrite horizons are generally reported to be vesicular and crystal-rich, with a mineral assemblage of sanidine, quartz, magnetite and amphibole (Teklemariam et al., 1996). The ignimbrites represent the main reservoir for the geothermal field (Fig. 2) and have undergone extensive hydrothermal alteration (Teklemariam et al., 1996). Note that previous authors commonly refer to this unit as 'Tertiary Ignimbrite'.

5.1.2. Bofa Basalts (Neogene-Quaternary undifferentiated basaltic lavas, Nqub)

Ignimbrite units are overlain by a sequence of coarsely porphyritic and aphanitic basaltic lavas with intervening scoria horizons, palaeosols and minor ash beds (the Bofa Basalts, Figs. 2, 3). Basaltic rock horizons are found in all deep wells and have a maximum thickness of ~1000 m in LA-3 (Teklemariam, 1996; Teklemariam et al., 1996). The Bofa Basalts represent sub-aerial eruptive sequences (lavas and scoria) rather than intrusive bodies (Teklemariam et al., 1996).

5.1.3. Lacustrine sediments (Quaternary deep well lacustrine sediments, Qdl)

Stratigraphically above the Bofa Basalts (Nqub) is a sequence of lacustrine sediments, predominantly mudstones and siltstones, that have been identified in all wells except LA-4 and LA-5 (Fig. 3, Teklemariam et al., 1996). The lacustrine sediments show spatial variations in thickness, becoming progressively thinner to the east of the Aluto complex (Gizaw, 1993; Gianelli and Teklemariam, 1993; Teklemariam et al., 1996; Hutchison et al., 2015). The maximum thickness of the lacustrine sediments is ~400 m in well LA-2 (Teklemariam et al., 1996). In the centre of the complex they have a thickness of ~80 m in well LA-8 (Mamo, 1985, Table S2) and 2 km east of this (traversing a major fault zone at Artu Jawe, Fig. 4) lacustrine sediments are absent in deep well LA-4 (Yimer, 1984, Table S1) and LA-5 (Gianelli and Teklemariam, 1993; Teklemariam, 1996). This pattern suggests considerable topographic offsets existed during lacustrine sediment deposition. Given the rift setting, it is assumed that deposition of the lacustrine sequences took place in a faulted environment and that the greatest thicknesses of sediments were established in the most downthrown blocks on the west side of the complex (Hutchison et al., 2015).

A number of wells on Aluto show trachytic units preceding and interbedded with the lacustrine sediments (Figs. 2, 3). Core and cutting samples reveal that these units are composed of grey, variably consolidated trachytes (including tuff, lava and breccia) with phenocrysts of

Fig. 4. Geological map of Aluto volcano produced through interpretation of remote sensing imagery with field validation. Projection is UTM (Universal Transverse Mercator) Zone 37 N, with the World Geodetic System 1984 datum. Coordinates are in meters. The new map builds on previous geological mapping of Aluto by Kebede et al. (1985) as well as maps of Quaternary lacustrine sediments presented by Benvenuti et al. (2002, 2013). Note the apparent lack of outcrop of units Qgei and Qcr is due to their limited exposure at the base of deep gorges, which are invariably covered by thick sequences of younger units. Outcrops labelled with a '?' were not visited during our field campaign and have been categorized on the basis of surface geological descriptions by Kebede et al. (1985); future mapping should aim to verify the relationship between these outcrops and the new stratigraphy. Local names that are referred to in text and subsequent figures are italicised. Faults have been mapped previously by Agostini et al. (2011) and Hutchison et al. (2015). Fumarole vents and hot spring locations are from Kebede et al. (1985). The deep geothermal wells are identified by blue circles and labels. White stars link to the key stratigraphic sections in Fig. 5A–M.

alkali feldspar (Mamo, 1985). Intense hydrothermal alteration has led to calcite, chlorite and smectite precipitation in these units (e.g., Teklemariam et al., 1996) greatly complicating interpretation of the original rock texture and their relation to the lacustrine sequences.

The lacustrine sediments and overlying ignimbrites (Section 5.1.4) are highly altered and rich in clay minerals (e.g., chlorite, illite and smectite) (Teklemariam et al., 1996). It is likely that these units provide a low porosity and low permeability clay cap layer that seals the Aluto-Langano geothermal reservoir (Fig. 2; Teklemariam, 1996).

5.1.4. Ignimbrites and trachytic tuffs (Qdt–Qgei)

Overlying the lacustrine sediments and Bofa Basalts are grey-green welded ignimbrites, variably consolidated tuffs and lithic breccias (Fig. 2, Teklemariam et al., 1996). The tuffs have a fine, devitrified groundmass, and contain sanidine phenocrysts as well as rhyolitic and trachyitic lithic fragments (Yimer, 1984; Mamo, 1985). The ignimbrite sequences are thickest in the centre of the complex where they are in excess of 300 m in well LA-8 (Mamo, 1985, Table S1).

5.1.5. Peralkaline rhyolites (Qcr–Qpoy)

The uppermost units found in the Aluto wells are peralkaline rhyolites (Figs. 2, 3), and include obsidian lavas, finely crystalline lavas and pumice breccias (Tables S1 and S2). There are no detailed descriptions of the sub-units within the peralkaline rhyolite sequence, and at present it is not possible to correlate sub-units (e.g., individual lava flow deposits) between the wells and assess lithological or thickness variations. Descriptions of well LA-4 by Yimer (1984) provide the most comprehensive account of the lithological sub-units within the peralkaline rhyolite sequence (Fig. 3, Table S1), but future work to systematically log these horizons is essential. Above the ignimbrite and trachytic tuff sequences (Section 5.1.4), Yimer (1984) identified flow banded comenditic rhyolites in a core cut at 256–266 m. Unfortunately, no cores were taken across the ~30 m transition from the major ignimbrites to the comendites, Table S1, leaving considerable uncertainty as to the nature of the contact between these units (Fig. 3, discussed in Section 8.2). Cuttings suggest that superposed on the comenditic rhyolites are ~50 m of pumiceous deposits and then ~30 m of aphyric obsidian lava (Yimer, 1984). The aphyric obsidian is then succeeded by ~40 m of sparsely porphyritic rhyolite lavas and finally, the upper most section comprises ~30 m of pumiceous breccias (Fig. 3).

5.2. Field stratigraphy

In the following sections we establish the field relations between the volcanic units exposed at the surface. Section 5.2.1 describes units that were identified off the main volcanic edifice in faulted sections around the margins of the Aluto complex; representative of the deepest accessible stratigraphy in the study region. Section 5.2.2 describes the succession of units identified on the main volcanic edifice, providing a complete sequence from the base to the top of the edifice. Finally, Section 5.2.3 describes the main sedimentary units as well as undifferentiated volcanic deposits. The key accompanying figures are: the synthetic stratigraphy of the surface volcanic units (Fig. 3, left-hand columns); the new geological map of Aluto (Fig. 4); graphic logs of key stratigraphic sections (Fig. 5) and annotated field photographs (Figs. 6 and 7). In addition, representative geochemical data for each of the main units are given in Table 2.

5.2.1. Off-edifice and uplifted volcanic units

5.2.1.1. Neogene-Quaternary undifferentiated basaltic lavas (Nqub). On the uplifted eastern flank of Aluto (Fig. 4) ~200 m of aphanitic and porphyritic vesicular basalt lavas were identified. The sequence comprises weathered basaltic lavas and breccias separated by minor palaeosols and scoriaceous horizons. East of Haroresa, south-east of the main edifice (Fig. 4) several large fault scarps ~100 m in height also reveal thick sequences of basaltic lava flow deposits comparable to those on the uplifted eastern flank of Aluto (Kebede et al., 1985). Blocks of basalt are identified as rare lithic clasts within PDC deposits on the main edifice suggesting that these units underlie the Aluto complex.

5.2.1.2. Quaternary trachytic tuffs and lavas (Qdt). Comenditic trachyte tuffs and lavas (Qdt), ~100 m thick, are exposed in fault scarps east of Lake Langano (at Mt. Dima, Figs. 4 and 5M). The trachytes are composed of both porphyritic and aphanitic types, and display varying degrees of vesiculation. Bright red blocky breccias are found between the layers of trachyte lava (Figs. 5M, 7A), suggesting that there were considerable hiatuses and periods of reworking between emplacement of the major lava flow units.

5.2.1.3. Quaternary grey welded ignimbrites (Qgyi). The next unit in the stratigraphic sequence is a package of strongly welded grey ignimbrites (Qgyi) that contain abundant lithic fragments and elongate fiamme (composed of partially devitrified obsidian). The welded ignimbrites (Qgyi) overlie the trachytic lavas (Qdt) at Mt. Dima (Fig. 4), although the contact was not clearly exposed (Fig. 5M). For the majority of Qgyi exposures only the grey densely welded zone of the ignimbrite is visible at the surface. Kebede et al. (1985) reported that in more complete sections the ignimbrites have a moderately compacted and poorly welded pumiceous base that grades upward into the densely welded zone before transitioning back into a non-welded pumiceous top. The thickness of this unit in well-exposed sections near Haroresa (Fig. 4) is ~50 m (Kebede et al., 1985).

5.2.1.4. Quaternary green welded ignimbrites (Qgei). Deposits of a welded green ignimbrite (map unit Qgei) are found in an uplifted fault block on the west of Aluto (Figs. 4, 5B). Qgei is composed of fine-grained pistachio-green matrix with dark grey fiamme and accessory lithic rock fragments (Fig. 7B). The stratigraphic context of Qgei is difficult to resolve owing to limited exposure; however at the type locality west of the edifice (Fig. 5B) it is immediately overlain by lacustrine sediments (siltstones, diatomite and reworked tephra) suggesting that it was emplaced in a lake basin. We frequently identified Qgei (and also Qgyi) as accidental lithic clasts within younger PDC deposits on the central edifice, suggesting that these two major ignimbrite units underlie the complex, and are considerably older than the volcanic units identified on the main edifice (Qcr–Qpoy, following section).

5.2.2. On-edifice volcanic units

5.2.2.1. Quaternary comenditic rhyolite (Qcr). The deepest deposits accessible on the main Aluto edifice are found at the base of Gebiba gorge on the south-east slope (Figs. 4, 5K, 6A). On the floor of the gorge the upper 5 m of a grey aphanitic lava (Qcr) is exposed. Qcr is a flow-banded comeditic rhyolite lava with large sanidine phenocrysts (1–3 mm diameter).

5.2.2.2. Quaternary aphyric obsidian (Qao). Overlying Qcr in Gebiba gorge is a ~ 10 m thick sequence of pumice, ash and breccia units (Fig. 6A). The contact between Qcr and the overlying volcaniclastic sequence is poorly exposed but taken to be unconformable (Fig. 5K). The volcaniclastic beds are themselves overlain by an obsidian lava flow deposit (Figs. 5K, 6A), which has a blocky aphyric obsidian surface and basal breccia (each ~2 m thick), and a ~ 7 m thick flow core comprised of finely crystalline rhyolite (Fig. 5K). The aphyric obsidian lavas and underlying bedded pumice are classified together as Qao. Qao lavas are dominantly exposed on the south-east slopes of the Aluto edifice where they cover an area of ~15 km^2 and extend for >7 km away from the centre of the edifice (Fig. 4).

5.2.2.3. Quaternary porphyritic obsidian (Qpo). The next phase of activity is represented by sparsely porphyritic obsidian lavas (Qpo), identified in

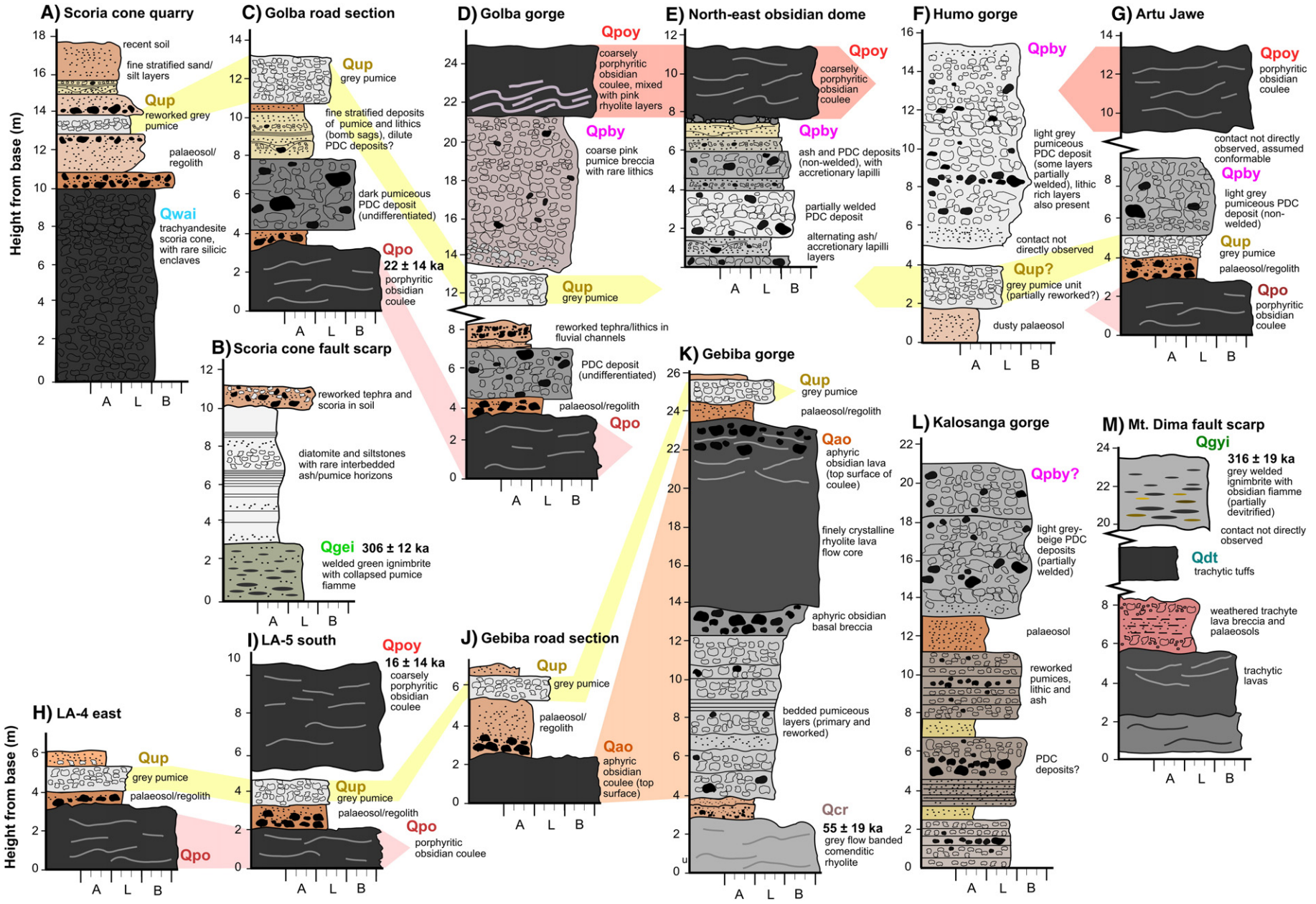

Fig. 5. Key stratigraphic sections used to constrain the eruptive stratigraphy (Fig. 3). Correlations are shown by the shaded colours that connect the sections. The location of each section is shown by the stars on the geological map (Fig. 4). Ages shown alongside the stratigraphy were determined by $^{40}Ar/^{39}Ar$ methods (Table 1 and Section 5.3). The bulk grain size of the volcaniclastic fragments in the deposit is given by the scale at the base of each section: A corresponds to ash, L to lapilli and B to blocks and bombs.

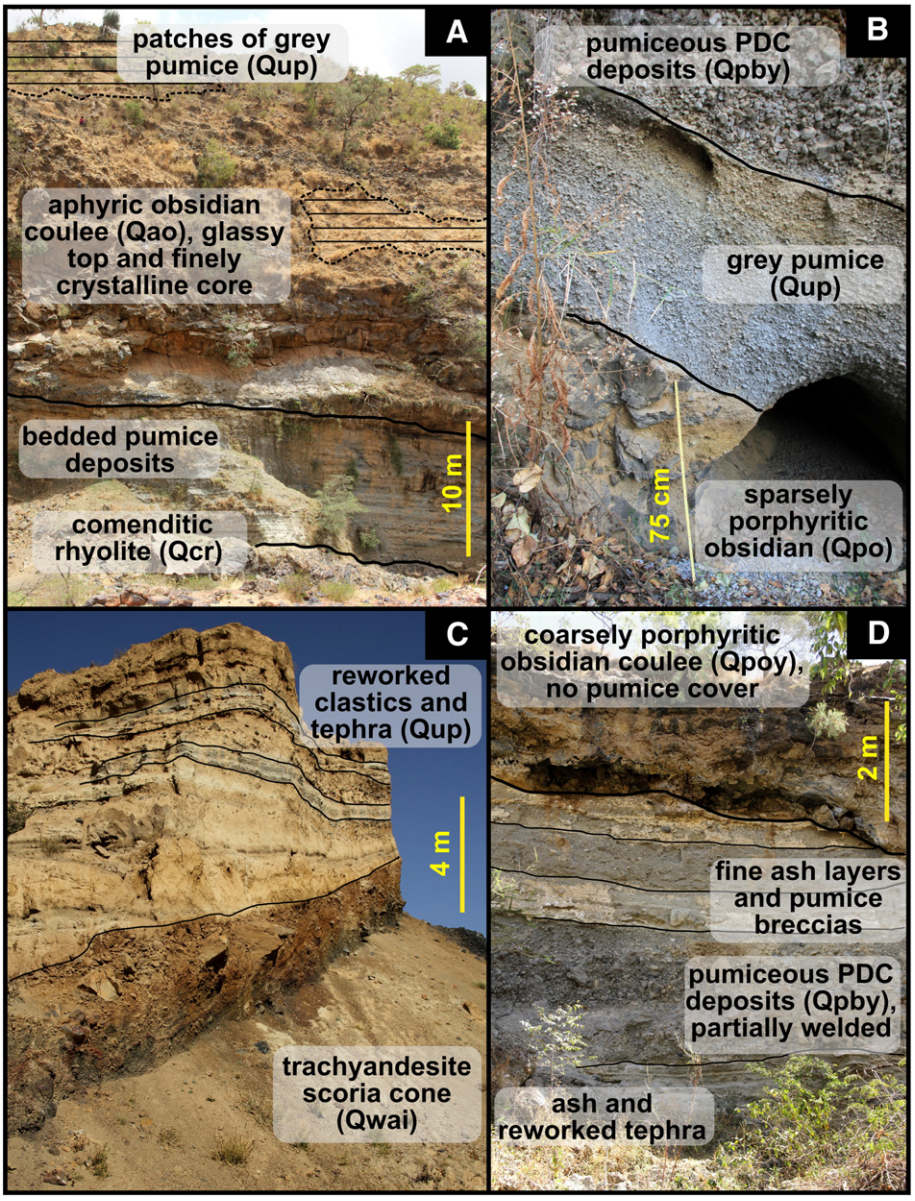

Fig. 6. Photographs of key stratigraphic sections. The photographs correspond with stratigraphic logs in Fig. 5 (A: Fig. 5K; B: Fig. 5G; C: Fig. 5A and D: Fig. 5E). The locations of the stratigraphic logs (which are tied to the photographs) are shown on the geological map in Fig. 4.

Figs. 5 (sections C, D, G, H and I) and 6B. A major dome of the Qpo unit is developed on the northern rim of the complex, where lavas extend ~2.5 km north of the volcanic vents (Fig. 4). Many of the Qpo lavas extend from breached craters suggesting that explosive phases preceded the lavas (although no underlying volcaniclastic units were exposed).

Obsidian lava flows Qpo and Qao are ubiquitously covered by soil horizons and tephra. Although we were unable to observe a direct contact between Qpo and Qao units it is evident from our field observations that soil horizons are thicker and more developed above Qao compared with Qpo (contrast Fig. 7C with Fig. 6B). We infer that Qao units were erupted earlier than Qpo lavas as shown in our stratigraphy in Fig. 3.

5.2.2.4. Quaternary west Aluto intermediate lavas (Qwai). Eruption of intermediate lavas is restricted to the west of the edifice (Qwai, Fig. 4). The main occurrence of Qwai is a small trachyandesite scoria cone, ~65 m high and ~600 m diameter, south of the main access road to Aluto from Adami Tullo (Figs. 4, 5A and 6C). The scoria cone is covered by a thin layer of pumice (Figs. 5A, 6C) suggesting it developed prior to the most recent explosive eruptive phases (Qup, next section).

5.2.2.5. Quaternary undifferentiated pumice (Qup). Covering all previously mentioned deposits of Aluto is an undifferentiated pale grey pumice deposit, Qup (Fig. 4, numerous sections in Figs. 5 and 6A–C). The thickness of the tephra varies across the complex from a few centimetres up to several meters where it has experienced reworking on steep slopes. The tephra comprises lapilli-pumice, and has rare chips of obsidian and hydrothermally altered material (<10 mm in diameter). Qup ubiquitously overlies palaeosols (e.g., Figs. 5, 7C) indicating that this unit marks the initiation of a major explosive eruption sequence. Field exposures (Figs. 6B, 7C) suggest that this unit is a single pumice fallout deposit, and likely to be the product of a (sub) Plinian eruption, but further work needs to be done to verify this.

5.2.2.6. Quaternary pumiceous breccias youngest (Qpby). Pumiceous breccias (Qpby) are encountered above the Qup tephra at Humo gorge and Artu Jawe (Figs. 5F, G and 6B, D). Qpby units were erupted from discrete

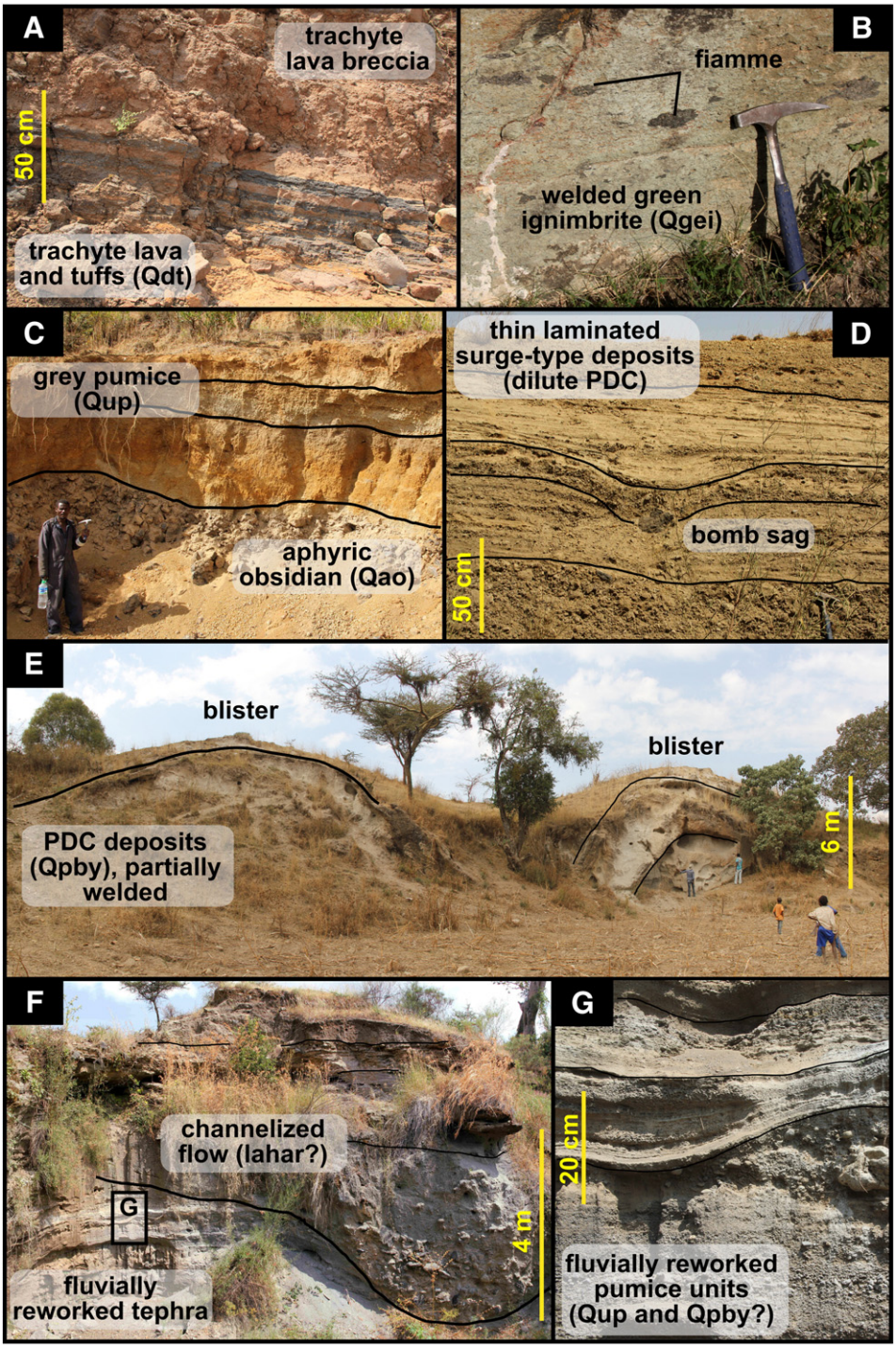

Fig. 7. Photographs showing field relations of key units. **A)** Trachytic lava breccias and tuffs (Qdt) exposed in uplifted fault blocks south-east of the Aluto edifice (Fig. 5M). **B)** Green welded ignimbrite (Qgei, from section Fig. 5B) with collapsed pumiceous fiamme, hammer for scale 0.30 m in length. **C)** Contact between aphyric obsidian lava (regolith) and light grey pumice unit (Qup) with ~1 m thick bright orange palaeosol developed (Fig. 5J). **D)** Section of explosive eruptions units, suggestive of phreatomagmatic processes (Fig. 5C). **E)** Hummocky 'blister' structures developed within a welded PDC deposit (Qpby, near Fig. 5F). **F)** Fluvially reworked tephras and volcaniclastic material deposited on the southern slope of the edifice, the large channel cutting down through the stratigraphy is typical of a lahar unit with a coarse lithic base load of obsidian cobbles. **G)** Detail inset from F), showing thin channels of reworked tephra (likely derived from units Qup and Qpby). Photographs F and G were taken ~1 km south-west of stratigraphic section 5 K (see Fig. 4).

vents across the complex and were not erupted in a single event (although some ignimbrites appear to have closely followed Qup with little evidence for any substantial hiatus, e.g., Fig. 6B). Qpby units have been emplaced as both PDCs (Fig. 6B, D) with run outs of several kilometres and localized pumice cones (Fig. 5D). The pumice cones comprise coarse (up to 300 mm diameter), clast-supported pumice exposures that have a mantle-bedded morphology (e.g., Golba gorge, Fig. 5D). Pumice cones are typically between 10 and 100 m in height, and may extend to ~1 km from the erupting vent; effusive obsidian coulees (e.g., Qpoy, next section) commonly follow, breaching the walls of the pumice cone.

Qpby PDC units, such as those identified at Humo gorge (Fig. 5F), show characteristic peralkaline ignimbrite textures with large pumice

Table 2
Geochemical overview of the main eruptive units. Major element concentrations are in wt.%, trace element concentrations are in ppm. Major elements were measured by XRF, trace elements were measured by either XRF or ICP-MS, as indicated by 1, 2 in the unit row, respectively. For the TAS subdivision row, P and C correspond to pantellerite and comendite respectively. TA stands for trachyandesite. The symbols represent ages from Teklemariam (1996) (†), Le Turdu et al. (1999) (+) and this study (*). n.d. stands for no data. For SO_3 b.d. indicates below detection limits. LOI: loss on ignition. NK/A: is an indication of peralkalinity and was calculated as molar $(Na_2O + K_2O)/Al_2O_3$ (e.g., Macdonald, 1974).

Unit		Nqui[1]	Nqub[1]	Qdt[2]	Qgyi[1]	Qgei[2]	Qcr[2]	Qao[2]	Qpo[2]	Qwai[2]	Qup[2]	Qpby[2]	Qpoy[2]
TAS subdivision		Rhyolite (C)	Basalt	Trachyte (C)	Rhyolite (P)	Rhyolite (C)	Rhyolite (C)	Rhyolite (P)	Rhyolite (P)	BTA	Rhyolite (P)	Rhyolite (P)	Rhyolite (P)
Type sample		S-1	S-2	15 02 09	18 11 07a/S-3	13 05 04	18 02 04	02 02 12	18 01 08	15 01 07B	03 02 23	30 01 06B	31 01 LE
Type location	**Lat (°N)**	Rift escarpment near Munesa	Eastern flank of Aluto complex	7.680784	7.69173	7.84068	7.74193	7.74960	7.83245	7.83979	7.81641	7.82314	7.78321
	Lon (°E)			38.806054	38.79719	38.73031	38.80486	38.80618	38.74576	38.72940	38.75248	38.78288	38.82680
Age (ka)		2300 ± 300 (†)	1600 ± 500 (†)	570–330 (+)	316 ± 19 (*)	306 ± 12 (*)	55 ± 19 (*)	n.d.	22 ± 14 (*)	n.d.	n.d.	n.d.	12 ± 7 (*)
SiO_2		70.21	49.76	65.18	69.92	71.13	70.02	72.68	73.15	59.85	70.86	72.41	73.56
TiO_2		0.50	2.86	0.89	0.44	0.34	0.43	0.30	0.22	1.64	0.17	0.23	0.32
Al_2O_3		12.23	16.79	15.46	10.37	11.46	12.08	10.03	8.88	15.13	7.78	9.05	9.78
FeO_t		5.85	11.56	5.72	6.74	5.21	5.57	5.25	5.82	7.32	6.48	5.37	5.03
MnO		0.17	0.17	0.22	0.27	0.22	0.19	0.22	0.25	0.14	0.32	0.22	0.22
MgO		0.30	4.15	0.59	0.21	0.10	0.10	0.00	0.00	2.53	0.00	0.00	0.00
CaO		0.13	7.83	2.14	0.54	0.39	0.18	0.24	0.20	4.83	0.14	0.20	0.22
Na_2O		4.06	3.28	5.46	5.98	5.79	5.32	6.15	6.31	4.64	6.69	5.22	5.80
K_2O		4.09	1.10	3.38	4.38	4.51	4.72	4.39	4.27	2.70	4.15	4.41	4.35
P_2O_5		0.03	0.62	0.21	0.02	0.02	0.01	0.01	0.01	0.27	0.01	0.01	0.01
SO_3		b.d.	b.d.	0.01	b.d.	b.d.	b.d.	b.d.	b.d.	0.06	b.d.	b.d.	b.d.
LOI		1.91	1.49	0.31	0.68	0.22	0.82	-0.22	-0.04	0.57	2.14	2.19	-0.40
Total		99.48	99.61	99.57	99.55	99.42	99.43	99.06	99.08	99.70	98.74	99.32	98.89
NK/A		0.91	0.39	0.82	1.41	1.26	1.15	1.48	1.69	0.70	1.99	1.48	1.46
Y		74	33	76	73	68	64	100	116	32	190	121	88
Zr		1156	285	627	992	838	787	942	1102	359	1655	1059	771
Nb		147	38	84	166	142	120	151	166	46	264	170	122
Rb		62	15	82	110	112	69	106	124	63	156	110	83
Sr		7	484	300	12	11	7	4	2	361	8	5	5
Ba		105	539	955	287	234	370	213	347	776	397	367	470
La		196	50	75	125	102	58	124	147	50	230	145	106
Ce		191	97	152	252	227	103	255	302	96	475	299	216
Cr		3	21	0	3	0	0	2	1	12	0	0	2
Co		10	41	4	12	4	4	10	9	21	0	0	13
Ni		5	17	0	3	0	0	0	1	7	1	0	1
V		4	281	9	5	6	2	0	0	180	0	0	0

clasts (50–300 mm diameter) and lithic-rich horizons set in a variably welded ashy matrix. North-east of Humo gorge, PDC deposits display hummocky ('blister') structures, 6–8 m in height, and 15–20 m in diameter (Fig. 7E). Ignimbrite blisters have been described at a number of other peralkaline systems (Gibson, 1969, 1970; Williams et al., 2004; Mundula et al., 2013) and are linked to gas coalescence and deformation of the ignimbrite upon emplacement and prior to cooling and solidification. Qpby deposits often contain accretionary lapilli (Fig. 5E), bomb sag structures and thinly stratified ash-lapilli horizons (Figs. 5C, 7D) indicative of surge-type (dilute PDC) deposits, as have been reported at many other silicic volcanoes (e.g., Santorini, Sparks and Wilson, 1990), and are suggestive of phreatomagmatic eruptive processes at Aluto.

Overall the Qpby units represent a mixture of volcaniclastic deposits that were either built up around erupting vents (pumice cones), or formed density currents during particularly explosive phases. Their general evolution and morphology is comparable to the silicic lava cones and shields described by Mahood and Hildreth (1986) at Pantelleria.

5.2.2.7. Quaternary porphyritic obsidian youngest (Qpoy). The youngest volcanic deposits of Aluto are coarsely porphyritic obsidian lavas (Qpoy, e.g., Figs. 5D, E, G, I; 6D). Unlike obsidian lava flow units Qpo and Qao, Qpoy lavas are not covered by soil horizons or tephra (compare Figs. 6B and 7C with Fig. 6D) and so they are easily distinguished as the most recent eruptive products (Fig. 3). Qpoy lavas range from ~200 m to ~2.5 km in length, and show marked differences in surface weathering, suggesting that they were not emplaced in a single eruptive event. Qpoy vents commonly coincide with volcanic or tectonic structures, such as the caldera ring fault or the Artu Jawe fault zone that runs NNE-SSW east of the caldera floor (Fig. 4, Hutchison et al., 2015).

5.2.3. Undifferentiated volcanic or sedimentary units

5.2.3.1. Undifferentiated volcanic units (Qutc and Nquw). North of the Aluto edifice we identify numerous tuff cones (map unit Qutc), around the shore of Lake Ziway (Fig. 4), and to the east of Aluto, we have mapped scoria cones and basaltic fissure lavas occurring in the Wonji fault belt (Nquw, Fig. 4). Given their proximity and comparable surface weathering to the volcanic deposits of Aluto we assume that these formed contemporaneously to the Aluto edifice; however, their precise relations to the proximal volcanic stratigraphy have yet to be constrained.

5.2.3.2. Pleistocene and Holocene lacustrine units (Qlp and Qlh). Lacustrine sediments (predominantly siltstone, sandstone and diatomite) deposited in the Ziway-Shala basin are found north, south and west of the main edifice (Fig. 4, Gasse and Street, 1978; Street, 1979; Le Turdu et al., 1999; Benvenuti et al., 2002, 2013). While previous authors (e.g., Benvenuti et al., 2002) have defined several unconformity-bounded units that record major stages in the lake evolution, we simply delineate the main boundary between Pleistocene and Holocene sediments (Qlp and Qlh, respectively) in our geological map (Fig. 4). The Holocene high-stand of the Ziway-Shala basin (between 10 and 5 ka) was 1670 m above sea level

(Benvenuti et al., 2002), and therefore sediments in the plains around Aluto that are below this height level are assumed to be Holocene in age. Conversely, sediments above 1670 m height are correlated to the Late Pleistocene Megalake phase deposited during the last glacial period, ~100–22 ka (Benvenuti et al., 2002, 2013). The deep gullies west of Aluto that drain into the Bulbulla river are an exception to this, where ~50 m thick sequences of Pleistocene lacustrine sediments have been described by Gasse and Street (1978), Street (1979), Benvenuti et al. (2002) and Ménard et al. (2014).

5.2.3.3. Reworked volcaniclastic sediments and colluvial-fluvial sediments (Qal and Qc). There is abundant evidence for fluvial reworking of volcaniclastic material on Aluto (map unit Qal). On the flanks of the main edifice, drainage networks are well developed and have reworked volcaniclastic material in both narrow streams (Fig. 7G) and large channels (potentially episodic lahars, Fig. 7F). The caldera floor of Aluto is a self-contained basin that has been infilled by reworked volcanic deposits derived from the rim of the complex (mostly rounded pumice lapilli as well as sand-silt size lithic fragments). It is possible that Aluto hosted a caldera lake during periods of humid climate, and this feature may explain the phreatomagmatic characteristics of PDC deposits reported in unit Qpby (Section 5.2.2).

East of Aluto undifferentiated terrigenous clastic sediments (gravel, sandstone, siltstone and mudstone) were identified (map unit Qc). These units are representative of colluvial and fluvial sedimentary facies deposited on the faulted margins of the Ziway-Shala lake basin.

5.3. Age constraints and correlations between the surface and deep stratigraphy

New and existing age constraints on volcanism are given in Table 1, and shown alongside our stratigraphic interpretations in Fig. 3. These units are discussed from the base to the top of the pile. The ignimbrite units (Nqui) found at the base of the deep wells lack robust age constraints, as K/Ar analysis of altered feldspars yielded a minimum age of 1.4 Ma (WoldeGabriel et al., 1990). Nevertheless, previous authors (e.g., WoldeGabriel et al., 1990, 1992; Teklemariam, 1996) have correlated the Aluto deep well ignimbrites (Nqui) with petrologically and geochemically analogous ignimbrites found near Munesa (Fig. 1B), which yielded ages of 3.51 ± 0.03 Ma (Munesa Crystal Tuff), 2.9 ± 0.3 Ma (Munesa Vitrophyre) and 2.30 ± 0.03 Ma (Neogene Ignimbrite). These correlations should be viewed with caution until further geochemical evaluation and age analysis is undertaken.

The next unit is Nqub, and on the on the basis of their comparable geochemistry, thicknesses and emplacement style, we correlate the surface exposures of basaltic lava (Nqub) with the Bofa Basalt unit described in the deep wells (Fig. 3, Table S1,2 and Gianelli and Teklemariam, 1993). The age of Nqub is constrained at 1.6 Ma ± 0.5 Ma by a K/Ar determination from a porphyritic basalt lava on the eastern flank of Aluto (Table 1, Teklemariam, 1996).

No direct ages are available for lacustrine sequences encountered in the deep wells (Qdl). These sequences appear to represent the oldest lacustrine sediments deposited in the Ziway-Shala basin (Fig. 1B), and probably have an age of ~570–330 ka (i.e., the maximum age range for the basin, Le Turdu et al., 1999).

Trachytic tuffs and lavas found at Mt. Dima (Qdt) are tentatively correlated with the trachytes identified in the deep wells (Fig. 3), on the basis of their similar deep position in the stratigraphy and their broad compositional similarity. Direct ages for trachyte lavas are still to be established, however their close association with lacustrine sediments (Section 5.1.3) would suggest that their ages are roughly equivalent (around ~570–330 ka), and indeed they must have erupted before ~310 ka, the age of the overlying ignimbrites.

The welded ignimbrite sequences, Qgyi and Qgei, yield overlapping $^{40}Ar/^{39}Ar$ ages of 316 ± 13 ka and 306 ± 12 ka (Table 1) and we correlate these units with the thick ignimbrite and tuff sequences described in the deep wells (Section 5.1.4, Fig. 3).

For the units on the main edifice of Aluto, our $^{40}Ar/^{39}Ar$ results support ages of the comenditic rhyolites (Qcr) at 54 ± 13 ka, the sparsely porphyritic obsidian coulees (Qpo) at 62 ± 13, 22 ± 14 and 19 ± 5 ka, and the youngest obsidian coulees (Qpoy) at 16 ± 14 ka (Table 1). West of Aluto, in the deep gorges of the Bulbula plain, Gasse and Street (1978) and Street (1979) identified numerous volcaniclastic horizons interbedded with lacustrine sediments and dated these using radiocarbon methods. The largest volcaniclastic sequence, informally known as the Abernosa pumice, was deposited between ~26 and ~14 cal. ka BP, and preserves ~13 distinct tephra layers (Gasse and Street, 1978). The youngest tephra layer to be identified by Gasse and Street (1978) shows a broad age overlap with the youngest tephra found south-east of Aluto at Haroresa (Benvenuti et al., 2013, Fig. 4), between ~11 and ~6 cal. ka BP (Table 1). As these deposits represent the youngest widely dispersed tephra we correlate these with Qup, the most recent pumice fall unit that we could identify on the main edifice (Section 5.2.2, Fig. 4). This correlation would suggest that the youngest eruptive products (Qpoy and Qpby) are younger than ~10 ka (Section 8.3), which is consistent within error of the $^{40}Ar/^{39}Ar$ for Qpoy. Finally, a radiocarbon age for charcoal found immediately beneath a thin bed of pumiceous pyroclastic deposits (20–30 cm thick) on the west of the Aluto edifice (Hutchison et al., in press) provides an age of 0.40 ± 0.05 cal. ka BP for the youngest explosive eruptions on the complex (unit Qpby, Fig. 3).

The ages also constrain Qao lavas between 74 and 49 ka and the Qwai scoria cone to >10 ka (i.e., older than overlying Qup, Figs. 3, 6C). In Fig. 3 probable links between the surface volcanic deposits on the main edifice and the peralkaline rhyolites in deep wells are shown, and were made on the basis of comparable lithological descriptions.

6. Petrography and Geochemistry

6.1. Petrography

Basaltic lavas from Aluto (Nqub and Nquw) are vesicular and variably porphyritic (0–40 vol.% phenocrysts) with holocrystalline matrix textures (Fig. 8A). The phenocryst assemblage is dominated by plagioclase, with subordinate olivine, clinopyroxene and Fe-Ti oxides (Fig. 8A). The minerals found in the matrix are equivalent to the phenocryst assemblage. Trachyandesite lavas (sampled from the scoria cone, Qwai, Fig. 6C) are highly vesicular, and aphyric to scarcely phyric, with microphenocrysts predominantly represented by plagioclase feldspar (Fig. 8B). Within the trachyandesite scoria cone (Qwai, Section 5.2.2) small (<10 mm) fragments of silicic rocks (possessing a granular texture, Fig. 8C) as well as partially resorbed xenocrysts of alkali feldspar (Fig. 8B, C) and aenigmatite are found mantled by the trachyandesite groundmass. The bulk geochemical composition of these silicic enclaves is comparable to the peralkaline rhyolites of Aluto (see Figs. 9–11, red star). The enclaves likely represent partially disaggregated xenoliths of intrusive silicic rocks or crystalline mush that was entrapped by the trachyandesite melt prior to eruption.

Welded ignimbrites contain large phenocrysts of alkali feldspar (10 vol.% in Qgyi and 30 vol.% in Qgei) as well as less common alkali pyroxene, aenigmatite and Fe-Ti oxides set in a devitrified groundmass (Fig. 8D). Rhyolite and trachyte lava xenoliths (10–30 mm in diameter) are common, as are finely crystalline fiamme (Fig. 8D) and collapsed vesicles.

Samples from obsidian coulees are either aphyric (e.g., Qao) or porphyritic (e.g., Qpo and Qpoy). Porphyritic obsidian samples contain phenocrysts of alkali feldspar, aenigmatite, alkali pyroxene (aegirine-augite), quartz, Fe–Ti oxides and rare amphibole (Fig. 8E). The porphyritic obsidians are typically glomeroporphyritic, and the glassy matrix contains aligned microlites of alkali feldspar, alkali pyroxene and aenigmatite (Fig. 8E). Quartz-feldspar granophyric textured

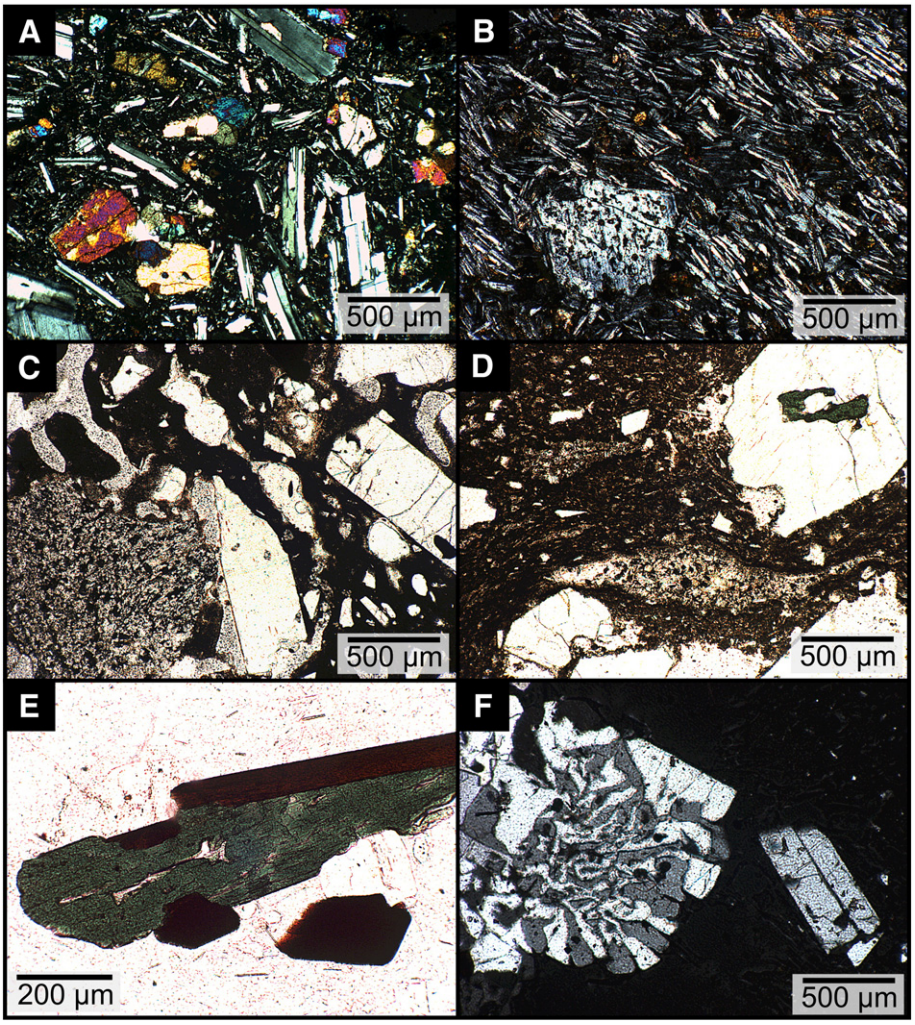

Fig. 8. Photomicrographs of key eruptive products. **(A)** Alkali basalt (Nquw, 17–01-05) sampled from a scoria cone north-east of the Aluto complex (shown in cross polarised light). The main phenocryst phases are plagioclase and olivine (note dark brown reaction rims on several grains). The phenocrysts are set in a fine grained (holocrystalline) groundmass also containing plagioclase and olivine as well as clinopyroxene and Fe-Ti oxides. **(B)** Trachyandestite (Qwai, 15–01-07B) sampled from a quarried scoria cone west of Aluto (shown in cross polarised light). The groundmass is dominated by aligned microphenocrysts of plagioclase. Rare, partially resorbed, sieve-textured crystals of alkali feldspar compositions are also present. **(C)** Silicic enclave (15–01-07 A) also sampled from the scoria cone (Qwai) west of Aluto (shown in plane polarised light). Partially-resorbed xenocrysts of alkali feldspar (lower centre and right) as well as granular silicic xenoliths are wrapped in dark brown trachyandestite glass. **(D)** Welded ignimbrite (Qgei, 13–05-04) shown in plane polarised light. While the rock appears green in field photographs (Fig. 7B) in thin-section the matrix appears orange-brown in colour and is composed of a very fine grained groundmass that has likely devitrified and altered significantly. Fiamme are visible in the lower centre of image and are composed of lenses of silicic material that are coarser than the groundmass. Alkali feldspar, the dominant crystal phase, show a large range in sizes and in some instances have trapped earlier crystallizing phases (note embayed alkali pyroxene inclusion top right). **(E)** Porphyritic obsidian (Qpoy, 01–02-13) sampled from the southern rim of the Aluto edifice (shown in plane polarised light). In the centre of the image the main phenocryst phases of aenigmatite (opaque to deep red or brown colour), alkali pyroxene (dark green) and alkali feldspar (low relief and colourless) can be identified. Note that the pyroxene is embayed and appears to be overgrown and replaced by the aenigmatite. The glassy matrix contains aligned microlites of alkali feldspar and alkali pyroxene. **(F)** Porphyritic obsidian (Qpo, 18–01-08) sampled from the north-west margin of the main Aluto edifice (shown in cross polarised light). A granophyric textured crystal (intergrowth of alkali feldspar and quartz) is visible on the left while a regular alkali feldspar crystal is shown on the right. The rectangular crystal form suggests that quartz is nucleating on the alkali feldspar. Granophyric textures are envisaged to form along the cooled walls and roof zone of the magma reservoir (e.g., Lowenstern et al., 1997).

intergrowths (1–3 mm diameter, Fig. 8F) were also identified in several porphyritic obsidian deposits and likely represent cognate xenocrysts (e.g., Lowenstern et al., 1997). Phenocryst content varies from 0 to 40% between the different obsidian lavas, and appears to be greatest in the youngest least weathered obsidian coulee (the eastern most Qpoy deposit, Fig. 4). Pumice deposits have similar crystal assemblages to their associated obsidian lavas although are generally lower in total phenocryst content (i.e., closer to aphyric).

6.2. Major elements

Rocks were classified using the total alkalis-silica (TAS) diagram (Fig. 9A, after Le Maitre et al., 2002). Note that in all geochemical plots (Figs. 9–12) we have adopted a colour scheme that differentiates the main eruptive units following the interpretations that were made in Section 5, and which we expand on further in Section 7. The major element data shows that the majority of volcanic rocks sampled at the surface of Aluto are of rhyolitic composition (Fig. 9A). Overall, there is a large range in silica content across the sample suite (SiO_2 43–76 wt.%) and there are representatives of each major compositional division, although rocks of intermediate composition are least abundant.

The silicic rocks of Aluto are represented by trachytes (Qdt), and rhyolites (all units on the main volcanic edifice, Qcr–Qpoy, as well as the welded ignimbrite units, Qgyi and Qgei). Silicic rocks were further classified as pantellerites and comendites according to the FeO_t – Al_2O_3 diagram (Fig. 9B) after Macdonald (1974). Trachytes (Qdt) are

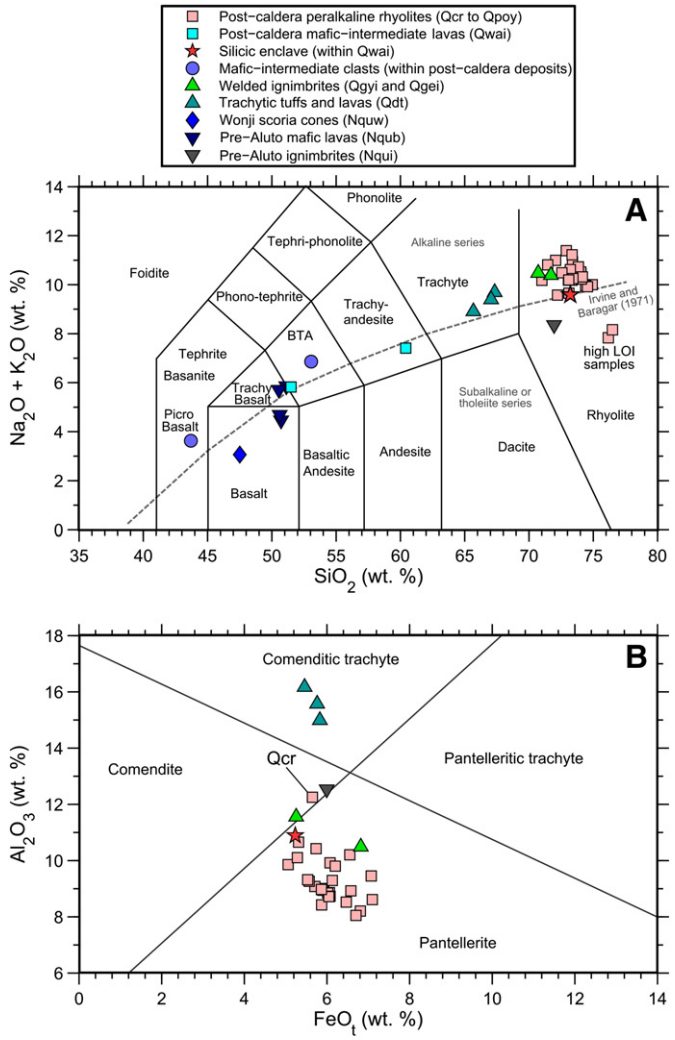

Fig. 9. Geochemical overview of Aluto volcanic rocks. **(A)** Total alkalis versus silica (TAS) diagram (Le Maitre et al., 2002). The grey dashed line shows the alkaline-sub-alkaline divide of Irvine and Baragar (1971). Two rhyolite pumice samples, discussed in text, show high loss on ignition (LOI) values and low Na_2O values suggestive of post-emplacement alteration. These samples have been removed from subsequent plots. **(B)** Classification diagram of peralkaline rhyolites and trachytes (Macdonald, 1974). Qcr corresponds to the comenditic rhyolite sampled from the base of the Aluto stratigraphy (the earliest post-caldera phase, Sections 5.2.2 and 5.3).

comenditic, welded ignimbrite units, Qgyi and Qgei, show pantelleritic and comenditic compositions respectively, and the bulk of post-caldera samples are pantelleritic rhyolites (the only exception is the comenditic rhyolite Qcr, found at the base of the main edifice, Section 5.2.2).

Two rhyolite pumice samples (17–01-01 K and 17–01-01G, Table S3) showed anomalously low Na_2O values (2.8 wt.%) and high loss on ignition (>5 wt.%) compared to other pumice samples (Table S3a); these samples are distinct outliers on the TAS diagram (Fig. 9A). Previous studies also identified anomalous low Na_2O values in seemingly pristine pumice samples (e.g., Peccerillo et al., 2003; Fontijn et al., 2013). These authors suggest that post-emplacement alteration processes (e.g., leaching by surface water interaction) may be the causal factor. Aluto samples that showed Na_2O loss were sampled from isolated pumice cones on the north-western periphery of the complex; these would have been located at the edge of the lake during lacustrine high stands (Gasse and Street, 1978; Le Turdu et al., 1999; Benvenuti et al., 2002, Fig. 4) and this may explain the alteration through interaction with surface waters. In all geochemical plots subsequent to Fig. 9A these altered samples have been excluded.

Analyses of mafic samples are limited to four Pre-Aluto (Nqub) units (Fig. 3), and a single Wonji lava (Nquw) sampled from a scoria cone ~10 km north-east of Aluto. The mafic units have a transitional composition and straddle the alkaline-subalkaline divide of Irvine and Baragar (1971) (Fig. 9A). A scoriaceous boulder of alkali picro-basalt composition was also sampled from a tuff cone (Qutc, at Adami Tullo, Fig. 4) by Di Paola (1972).

Intermediate products (SiO_2 52–65 wt.%) are restricted to the post-caldera intermediate units (Qwai, Section 5.2.7) and a lithic clast of basaltic trachyandesite composition (Fig. 9A) sampled from within a young PDC deposit (Qpby).

Major elements (Fig. 10) have trends characteristic of protracted fractional crystallization processes controlled by removal of olivine, clinopyroxene, plagioclase, Fe-Ti oxide, quartz, alkali feldspar and aenigmatite (in approximate order of appearance). TiO_2, FeO_t, MgO and CaO all decrease with increasing SiO_2 (i.e., they behave compatibly with increasing fractionation). K_2O has a smooth linear increase. Al_2O_3 has values of ~15 wt.% in the mafic to trachytic units but decreases to 8–12 wt.% in the rhyolite units, highlighting the onset of plagioclase feldspar as the major fractionating phase after ~67 wt.% SiO_2. Na_2O shows a generally increasing trend from mafic through to trachytic samples, and then considerable variation (5–7 wt.%) in the rhyolites. The variation in Na_2O after ~72 wt.% SiO_2 reflects the dominance of alkali feldspar as a fractionating phase (Section 6.1). P_2O_5 shows a general decrease with increasing SiO_2 but with a significant inflexion at ~55 wt.% SiO_2 (P_2O_5 behaviour likely reflects late fractionation of apatite; although rare it is likely to be an accessory phase throughout the crystallizing sequence, e.g., Field et al., 2013).

6.3. Trace elements

Selected trace elements and incompatible element ratios are presented in Fig. 11. The bulk of our new trace element data were determined by ICP-MS, although for two samples (13–05-04: unit Qgei, 15–02-09: unit Qdt) certain incompatible element values were above the analytical range at the time of measurement (Table S2c). In these cases we have plotted the equivalent trace element concentration determined by XRF (Table S3b). For elements analysed by both methods results compared well (<10% deviation between ICP-MS and XRF values for identical samples) and are within the uncertainty of measurements (Section 3). We have also included trace element data for three samples from Teklemariam (1996) in Fig. 11. Trace element concentrations of these samples (S1: unit Nqui, S2: unit Nqub and S3: unit Qgyi, Table S2d) were determined by XRF methods and because identical samples and standards were not run between our and their analysis we have been cautious not to interpret anything beyond the broad geochemical trends.

Sr does not change significantly from basaltic through to the intermediate and trachytic lavas but shows a marked depletion in rhyolites (Fig. 11); indicative of high degrees of feldspar removal. Ba shows an increase from basalts to trachytes before showing a marked inflexion at ~700 ppm Zr due to the appearance of alkali feldspar as a major fractionating phase in the rhyolites.

Incompatible elements (Y, Nb, La, Rb and Zr) reveal a near continuous fractionation sequence of Aluto lavas, the only significant gap occurs between Zr values of 450–700 ppm where only one representative trachyte sample exists. Incompatible-incompatible element diagrams (Fig. 11, Y, Nb, La and Rb against Zr) show smooth linear positive trends that pass through the origin, and are consistent with Aluto's evolved pantellerites being derived from a mafic parent with similar chemistry to the pre-Aluto (Nqub) or Wonji lavas (Nquw). The post-caldera rhyolites cover a considerable range in incompatible element values and the most evolved samples are from the grey pumice unit Qup (Section 5.2.2) which has 1650 ppm Zr. Notably, the comenditic rhyolite unit (Qcr), the earliest recognizable phase of post-caldera volcanism, is offset from the main fractionation trend for certain incompatible trace-

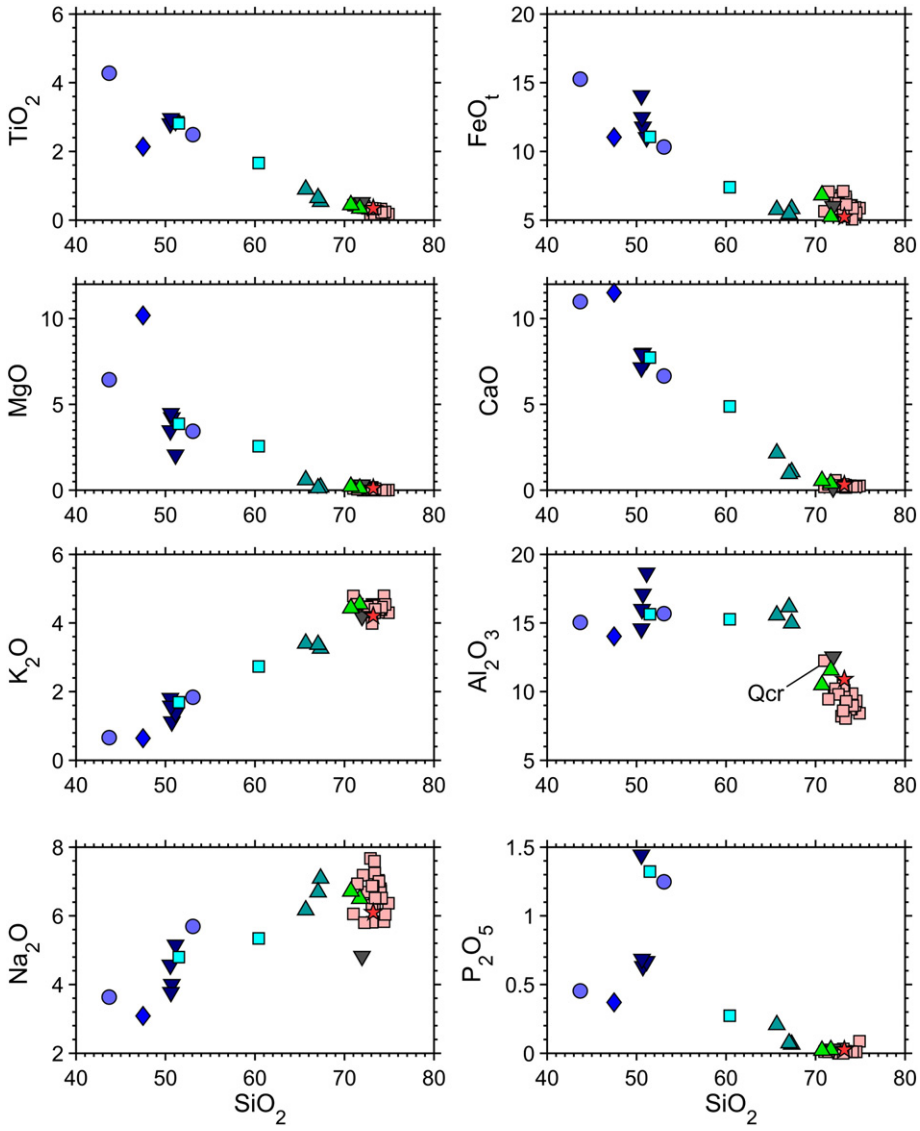

Fig. 10. Harker variation diagrams of whole-rock compositions determined by XRF. All concentrations are shown in wt.%. Key as for Fig. 9. Qcr corresponds to the comenditic rhyolite sampled from the base of the Aluto stratigraphy (the earliest post-caldera phase, Sections 5.2.2 and 5.3).

elements (e.g., Y and La against Zr, Fig. 10). An ignimbrite sampled from a fault scarp near Munesa (Fig. 1B) by Teklemariam (1996) that we classify as a Pre-Aluto ignimbrite (Nqui) also falls off the main linear array evidencing a different fractionation trend from the Aluto sample suite.

Ratios of incompatible elements such as La/Y and Rb/Nb (Fig. 11) do not show significant variations within the sample suite, and indeed the post-caldera rhyolites (excluding Qcr) show an exceptionally constant ratio. The Rb/Nb ratio of Precambrian crustal rocks, which represent a likely component of the basement rock, are much higher than any samples from Aluto (Fig. 11). We follow previous arguments of Peccerillo et al. (2003) and suggest that partial melting of these crustal rocks would tend to increase the large ion lithophile element and high field strength element ratios (LILE/HFSE, e.g. Rb/Nb in Fig. 11) in the melt, making it extremely unlikely that the peralkaline magmas were derived from crustal anatexis alone (discussed further in Section 8.1).

6.4. Examining fractional crystallization processes

Major and trace element trends are indicative of fractional crystallization (Sections 6.2 and 6.3). To assess the viability of this process in generating the Aluto sample suite we adopt the simple approach of Blundy and Wood (1991), and model evolving Sr concentrations in a melt governed by feldspar fractionation. From our petrographic observations (Section 6.1) it is clear that feldspar is the main phenocryst phase found throughout the sequence, and assuming that the system is dominated by feldspar fractionation then the progressive change in composition from anorthite to albite to anorthoclase (and the corresponding increase in the feldspar-melt partition coefficient, D_{Sr}) should explain the Sr whole-rock trends (e.g., Blundy and Wood, 1991).

In the model Zr is taken to be completely incompatible (in line with trace element observations in Section 6.3 and the lack of zirconium-bearing minerals observed petrographically) and is used as a proxy for melt fraction (F). The Wonji basalt sample (Nquw) which is poorly evolved and least enriched in incompatible trace elements (161 ppm Zr) is our best estimate of a parental magma, and we use Zr_{parent} / Zr_{sample} as an indicator of the fraction of liquid remaining. In the model we also assume that the partitioning of Sr between plagioclase feldspar and silicate melt (D_{Sr}) as a function of anorthite (An) content and temperature, as described by Blundy and Wood (1991), is the only process controlling Sr evolution in the melt. For each calculation we crystallize 10% of the residual liquid, and the temperature and An content of plagioclase are adjusted at each step (as shown in Fig. 12 A

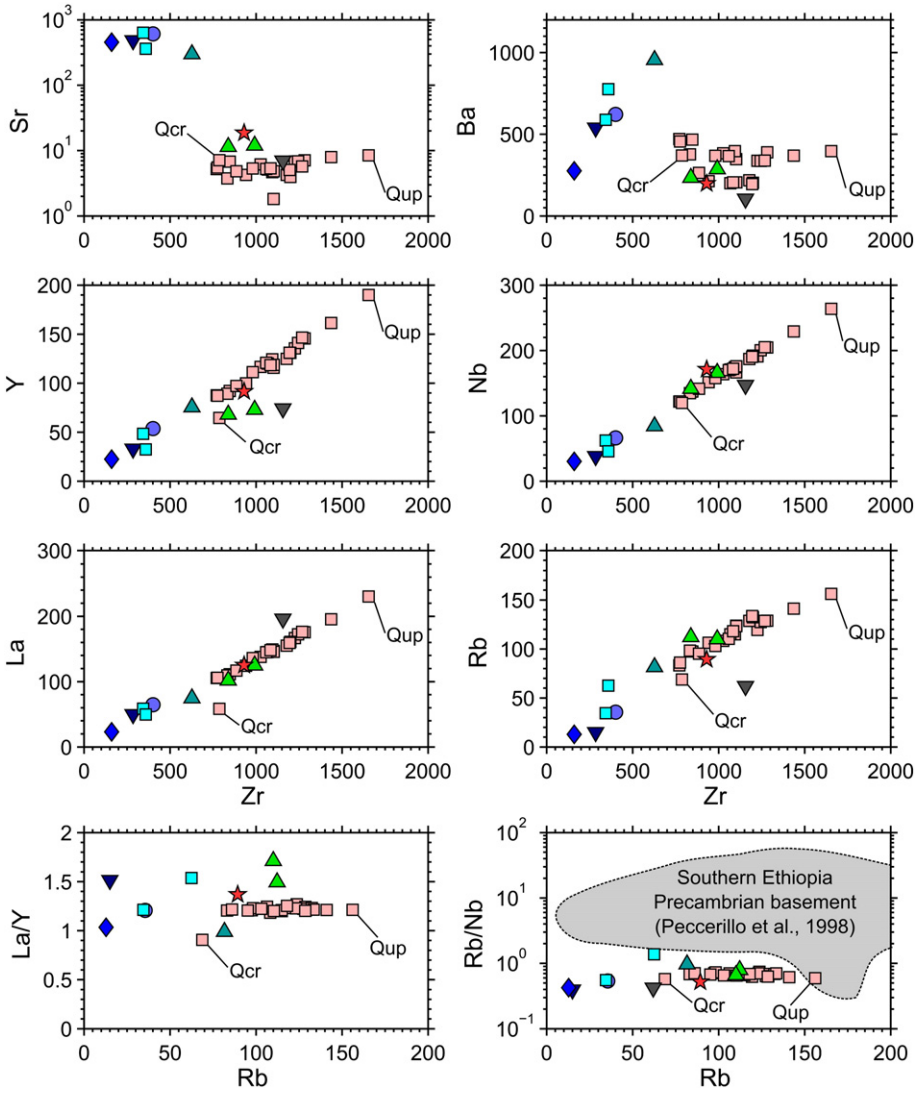

Fig. 11. Whole-rock trace element variation diagrams plotted against Zr (upper six plots) and Rb (lower two plots). All concentrations are shown in ppm. These represent whole-rock values determined by both XRF and ICP-MS methods (see text for discussion of compatibility). Key as for Fig. 9. Qcr corresponds to the comenditic rhyolite sampled from the base of the Aluto stratigraphy (the earliest post-caldera phase, Sections 5.2.2 and 5.3). Qup corresponds to the pumice fall deposit (Section 5.2.2). Precambrian basement trace element data are from Sidamo, Southern Ethiopia (Peccerillo et al., 1998).

and B). The temperature changes linearly from 1150 °C to 650 °C with fraction of liquid remaining (Fig. 12A), while the An content of plagioclase varies from An_{90} to An_{20} (Fig. 12B). These assumptions are based on petrological constraints of magma temperatures and mineralogy variations from Dabbahu volcano (Ethiopia) after Field et al. (2013); the only peralkaline volcano in the region where these detailed constraints exist. Four different fractionation trends are considered (Fig. 12C–E) each representing a constant percentage of plagioclase in the crystallizing assemblage (30%, 50%, 70% and 90% are shown). The resultant change of the bulk partition coefficient (D_{Sr}) is shown in Fig. 12C, and modelled melt Sr evolution is compared to the Aluto whole-rock data in Fig. 12D, E.

The Aluto whole-rock Sr values broadly match the melt evolution predicted by the models (Fig. 12D, E), although there is an obvious gap in samples between the trachytes and the least evolved rhyolite (i.e., the silicic enclave sampled from the scoria cone sequence, shown as the red star). The key observation from Fig. 12D is that it is possible to link back the peralkaline rhyolite Sr concentrations to the least evolved basaltic lavas via feldspar fractionation and this lends support to fractional crystallization being the dominant process in controlling melt evolution at Aluto. The models suggest that the total amount of fractional crystallization required to generate the peralkaline rhyolites from parental basaltic lavas is >80%, and that feldspar must be the dominant phase in the crystallizing assemblage (≥50%) in order to generate the rhyolites (in agreement with petrological observations made in Section 6.1). A key implication of this model, and the trace element diagrams in Fig. 11, is that degree of differentiation has changed through time. The welded ignimbrites are more chemically evolved than the trachytes, while the post-caldera magmas have undergone even more extreme fractionation. In Section 8.1 we consider petrogenesis and melt evolution processes at Aluto further, as well as future work that will be necessary to test our hypotheses.

7. Evolution of the Aluto Volcanic Complex

Using our new stratigraphic and age constraints we present a conceptual model outlining the development of the Aluto complex within the context of the evolving rift (Fig. 13).

7.1. Pre-Aluto ignimbrite units (4–2 Ma)

Rifting of the CMER in the Pliocene and into the earliest Pleistocene (before 2 Ma) was characterized by displacement along ~50 km long, widely spaced, NE-SW border faults (Bonini et al., 2005; Corti, 2009;

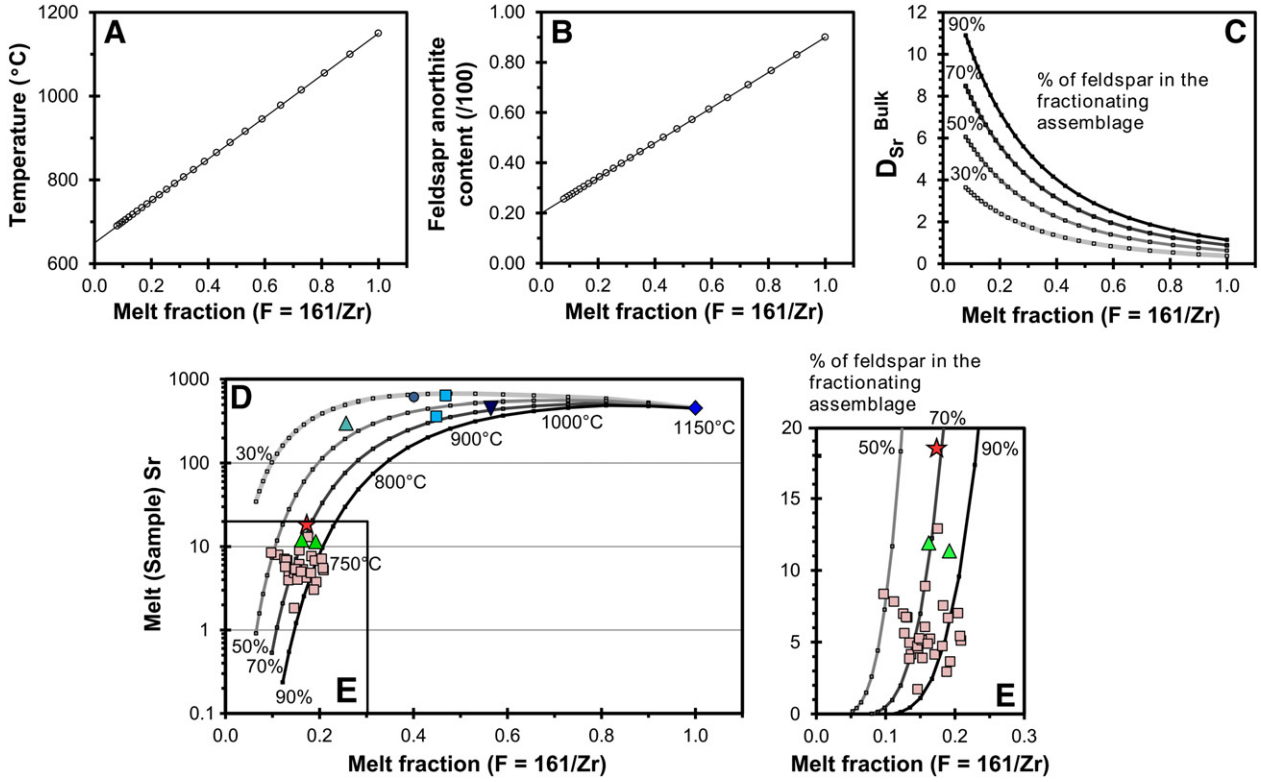

Fig. 12. Melt models to predict Sr concentration in a feldspar-dominated crystallizing assemblage using Zr as a proxy for melt fraction. We assume that the poorly evolved Wonji basalt (Nquw), which is least enriched in incompatible trace elements, is representative of a parental magma. The modelled temperatures, anorthite-content and the calculated bulk partition coefficient (D_{Sr}), are plotted in **A–C**, respectively. For each increment we crystallize 10% of the residual melt relative to the previous step. We consider four models where proportion of plagioclase as a percentage of total phenocrysts is held constant at 30, 50, 70 and 90%. **D)** Variation in Sr content of Aluto samples during fractionation (coloured points), compared to the modelled melt evolution trends (shown as lines where each point represents 10% crystallization of residual melt relative to the previous step). Data are plotted using the coloured symbols (see Fig. 9 for legend). **E)** Shows inset from D with a linear vertical scale.

Agostini et al., 2011). Volcanic activity was diffuse and silicic complexes were developed across a wide footprint of the rift (e.g., Mohr and Potter, 1976; WoldeGabriel et al., 1990). The oldest deposits identified in the Aluto deep wells are thick sequences of silicic ignimbrites (Nqui, Fig. 3). Hydrothermal alteration of these deep well units is extensive and greatly complicates thorough geochemical correlations and geochronological analyses (WoldeGabriel et al., 1990). The Nqui ignimbrites are presently constrained to be >1.4 Ma in age (Table 1), and in line with field correlations made by WoldeGabriel et al. (1990) and Teklemariam et al. (1996) we speculate that they derive from voluminous explosive eruptions at large axial volcanic complexes of Munesa (WoldeGabriel et al., 1990, 1992) and Gademotta (Laury and Albritton, 1975; Vogel et al., 2006), as well as the off-axis complexes (Mohr and Potter, 1976) which were all active within this time frame (Fig. 13A).

7.2. Rift localization and associated basaltic fissure eruptions (2–0.5 Ma)

A major shift in the style of rifting took place in the CMER after ~2 Ma (Boccaletti et al., 1998; Ebinger and Casey, 2001; Bonini et al., 2005), when deformation localized into axial volcanic segments (Corti, 2009; Agostini et al., 2011; Keir et al., 2015). Large volumes of mafic magma have been intruded into the roots of these segments (up to depths of ~10 km, Keranen et al., 2004) and in the brittle upper-crust above these intrusions faulting and dyking facilitate extension (Keir et al., 2006, 2015). Short (<20 km long), NNE-SSW trending, closely spaced Wonji faults (Fig. 13B) characterize tectonic deformation at the surface of these segments (Ebinger and Casey, 2001; Keir et al., 2015).

The >500 m thick sequences of sub-aerial basalt and trachybasalt units (Nqub, Figs. 3, 8), dated at ~1.5 Ma (Table 1), coincide with this major shift of deformation within the rift valley. Our interpretation is that these mafic lavas and scoria deposits relate to fissure eruptions occurring along the rift axis in tandem with Wonji fault development (Fig. 13B, analogous to present day rift-related volcanism in Afar, Ferguson et al., 2010). The great thickness of the mafic units as well as the occurrence of intervening palaeosol layers, suggests that Nqub sequences were generated from numerous eruptive events over a protracted timespan from around 1 Ma to ca. 100 ka.

7.3. Basin development and growth of the trachytic edifice (500–310 ka)

Following the mafic fissure eruptions, deep wells on the west of Aluto record lacustrine sediments accumulating within the fault controlled Ziway-Shala basin (which formed between 570 and 330 ka, Le Turdu et al., 1999, Fig. 13C). A number of the deep wells also show trachytic tuffs and lavas interbedded with the lacustrine sediments (Section 5.1.3, Fig. 3). The deep well trachytes are correlated with the trachytic units found at Mt. Dima (Qdt, Figs. 3, 4, 5M), and mark the onset of silicic volcanism in the region (i.e., they represent the earliest eruptive products of the Aluto volcanic complex). Our interpretation is that trachyte lava flows and tuffs built up a low relief silicic complex (or lava shield) upon the faulted rift terrain. Trachytic lava piles, as envisaged here (Fig. 13C), appear to commonly form the earliest growth stages of peralkaline volcanic edifices in both the Ethiopian and Kenyan rift systems (e.g., Shala: Mohr et al., 1980, Kone: Rampey et al., 2010, Emuruangogolak: Weaver, 1977; Macdonald, 2012, Menegai: Leat et al., 1984; Macdonald et al., 1994, Olkaria: Clarke et al., 1990;

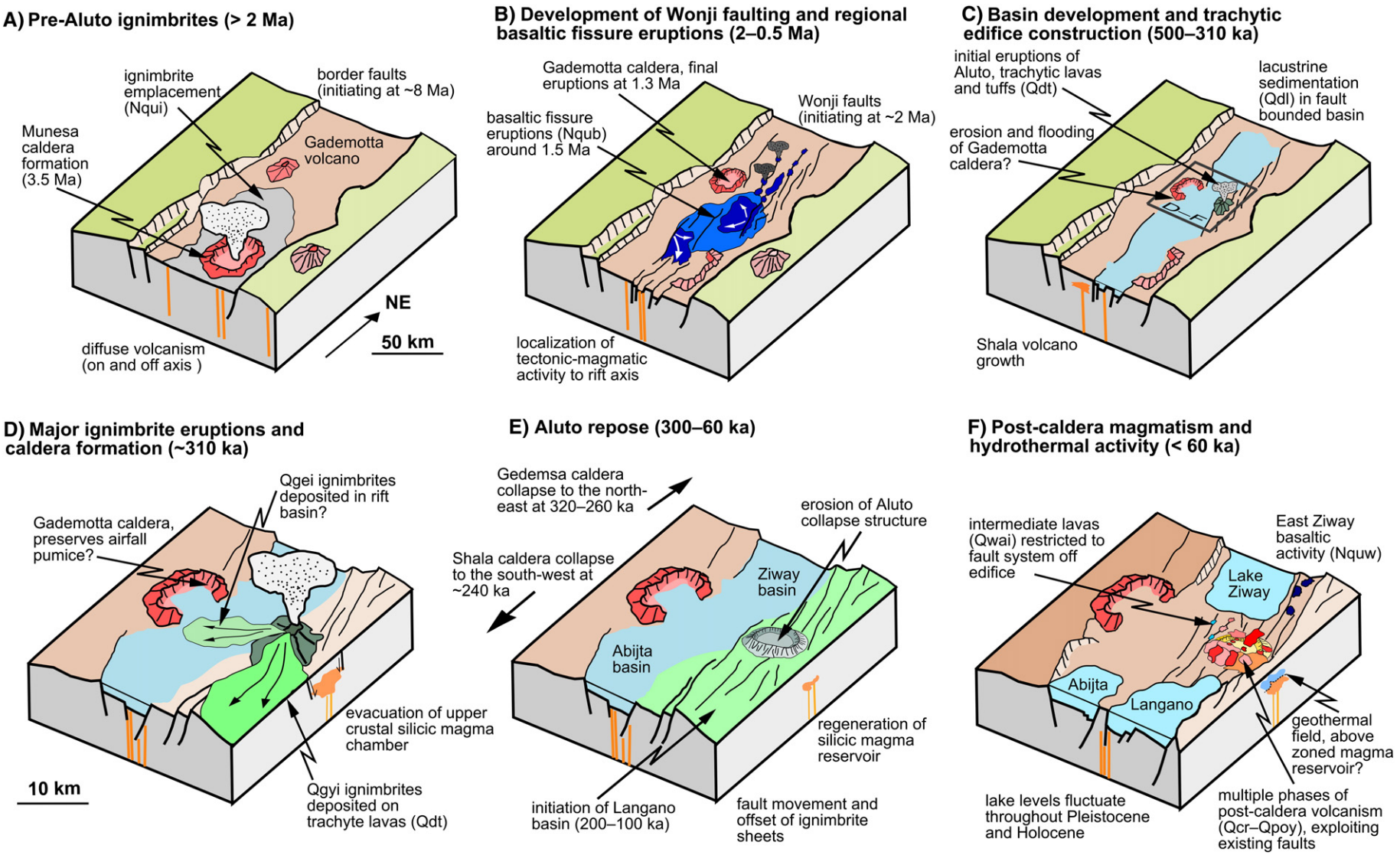

Fig. 13. Schematic diagrams depicting our proposed evolution of the Aluto volcanic complex within the context of the evolving Ziway-Shala rift basin as described and evidenced in the text.

Macdonald et al., 2008 and Longonot: Scott, 1980; Clarke et al., 1990; Scott and Skilling, 1999; Macdonald et al., 2014).

7.4. Climactic caldera-forming eruptions (~310 ka)

Caldera formation at peralkaline volcanoes is typically linked to explosive eruptions that generate widespread tuff sheets (e.g., Green Tuff, Pantelleria, Mahood, 1984; Mahood and Hildreth, 1986; Williams et al., 2013). At Aluto, the remnant caldera wall structure (Fig. 4), as well as constraints from soil-CO_2 degassing and vent alignments (Hutchison et al., 2015) all suggest that the complex has undergone at least one caldera-forming eruption. The welded ignimbrite units Qgei and Qgyi have overlapping $^{40}Ar/^{39}Ar$ ages of 316 ± 13 ka and 306 ± 12 ka (Fig. 3, Table 1), and represent the best candidates for widely dispersed, explosive ignimbrite sheets associated with a classic peralkaline caldera collapse (Fig. 13D). While there is insufficient field evidence to assess how these deposits physically relate (e.g., whether the ignimbrites represent one or multiple eruptive events), their componentry (large obsidian and pumice fiamme, of diameter > 100 mm), thicknesses (>10 m) and dense welding suggest that they are the proximal deposits of large-scale ignimbrite-forming eruption(s).

7.5. Volcanic hiatus at Aluto (300–60 ka)

Following the major ignimbrite eruptions at Aluto there appears to have been a significant hiatus (~250 ka) in volcanic activity (Fig. 13E). During this period major ignimbrite eruptions and caldera collapse took place at neighbouring volcanoes of Gedemsa: 320–260 ka; Shala: 240 ± 30 ka and Corbetti: 182 ± 28 ka (Mohr et al., 1980; Peccerillo et al., 2003; Hutchison et al., in press). At ~100 ka the Langano basin developed south of Aluto (Fig. 13E, Le Turdu et al., 1999) establishing a single deep freshwater lake in the region (Benvenuti et al., 2002).

7.6. Post-caldera activity (<60 ka)

Volcanic activity resumed at Aluto after ~60 ka (Fig. 3), and has been marked by the eruption of rhyolite lavas flows, pumice fallout and PDCs from vents largely confined to the main edifice (Fig. 13F). Our mapping allowed us to classify four distinct eruptive sequences, each bounded by palaeosols that mark pauses in volcanic activity (Fig. 3). The earliest phase consists of the comenditic rhyolite lavas (Qcr) which erupted at 55 ± 19 ka (Table 1). The next phase is represented by bedded pumice deposits and aphyric obsidian lavas (Qao). No ages have been determined for Qao, but this unit is stratigraphically bracketed between 74 and 49 ka. Subsequent eruptions comprise a series of sparsely porphyritic obsidian lava flows (Qpo) with ages of 62 ± 13 ka, 22 ± 14 ka and 19 ± 5 ka (Table 1). The most recent eruptive phase likely initiated after 10 ka (Section 5.3) and relates to volcanic units Qup–Qpoy. The youngest eruption of Aluto took place several hundred years ago at 0.40 ± 0.05 cal. ka BP (Fig. 3, Table 1).

Silicic eruption cycles for the post-caldera phases appear to initiate with an explosive eruption building small pumice cones and/or emplacing PDC deposits; these are then followed by effusive eruptions comprising obsidian or finely crystalline rhyolite lavas (e.g., Figs. 5E, K and 6A, D). This cyclic activity is consistent with a scenario where volatile rich magmas accumulate in the roof of the magmatic reservoir, overpressure triggers eruption of a gas-rich pumice units which are then followed by degassed obsidian coulees (in line with typical models of rhyolite lava dome emplacement from elsewhere, e.g., Mono Craters, California, Fink (1980), and Pantelleria, Mahood and Hildreth, 1986).

While we have classified four post-caldera eruptive phases, the field evidence from the youngest pumice breccias and obsidian lavas (Qpby and Qpoy), as well as the $^{40}Ar/^{39}Ar$ ages for Qpo units (Fig. 3, Table 1), demonstrate that individual lavas are erupted from discrete vents across the complex over a prolonged period of time. Therefore the mapped eruptive phases represent a sequence of rhyolite lava dome events, rather than a single eruption from a single vent. Volcanic vent locations, particularly for the youngest obsidian coulees (Qpo and Qpoy) are commonly linked to a structural control imposed by the underlying caldera ring fault or tectonic faults (Hutchison et al., 2015). Small volume intermediate eruptions (<0.01 km^3) have occurred on Aluto but are restricted to the faulted zones on the western flank (Figs. 4; 12F). Phreatomagmatic eruptions are also a common feature of volcanism in the last 60 ka (Fig. 7D), these would have occurred around the flanks of the volcano at the shoreline of the Ziway-Shala lake, but also potentially within the caldera when rising magma interacted with water stored in a caldera lake or geothermal reservoir.

8. Insights into Silicic Peralkaline Volcanism in Ethiopia

8.1. Geochemistry and magmatic evolution

The geochemical results and trace element modelling for the Aluto whole-rock suite (Section 6) are consistent with fractional crystallization as the fundamental process generating the evolved peralkaline melts erupted from the complex. This agrees well with geochemical and petrological arguments, modelling and experiments reported by several authors for the MER (e.g., Caricchi et al., 2006; Peccerillo et al., 2003, 2007; Ronga et al., 2009; Rooney et al., 2012; Giordano et al., 2014), as well as for other basalt–trachyte–pantellerite suites in comparable geodynamical contexts (e.g., Dabbahu, Barberi et al., 1975; Field et al., 2012, (2013) and Pantelleria, Civetta et al., 1998; White et al., 2009; Neave et al., 2012).

It has been argued that crustal assimilation may play a significant role at a number of other peralkaline centres (Davies and Macdonald, 1987; Black et al., 1997; Bohrson and Reid, 1997; Trua et al., 1999), however, based on characteristic trace element signatures (e.g., Rb/Nb Fig. 11) we suggest there is no requirement for any significant contribution from crustal melting to form the post-caldera rhyolites at Aluto. A more stringent test for crustal assimilation at Aluto will require additional radiogenic isotope analysis (Sr-Nd-Pb) and would be greatly complemented by a better understanding of lithospheric structure and composition in the CMER (e.g., Cornwell et al., 2010). Indeed at Fantale and Gedemsa volcanoes (also located in the MER), Giordano et al. (2014) found isotopic evidence for minor (~2%) crustal assimilation in mafic magmas as well as low temperature contamination of rhyolites by hydrothermal/meteoric fluids. It is important to recognize that while our results suggest fractional crystallization processes dominate at Aluto (Figs. 9–12), minor assimilation and contamination cannot presently be ruled out.

Understanding how the silicic melt reservoirs of the MER were assembled and the timescales over which this occurred is a major challenge, but nonetheless essential if we wish to achieve a complete synthesis of the magmatic processes that have operated during rift evolution. At Aluto, a great thickness (>500 m) of mafic lavas (Nqub) were erupted regionally prior to the formation of the silicic complex (Fig. 13B), and our trace element geochemistry (Section 6.3) and modelling (Section 6.4, Fig. 12) leads us to hypothesize that the mafic lavas are part of the same magmatic lineage as the peralkaline rhyolites. At present geochemical analyses of primitive mafic lavas from Aluto are extremely limited (Figs. 9–11) and further sampling, ideally complemented by melt inclusion studies, will be necessary to verify how representative our choice of parental melt composition is (Section 6.4).

Linking the Nqub basaltic lavas and the peralkaline rhyolites of Aluto as a single lineage, would suggest they were both generated from the same mantle-derived basaltic melt. We envisage a scenario where basaltic parental melt flux out of the MER mantle reservoir was focused into the axial volcanic segments of the rift zone (Section 7.2). Mantle-derived basaltic melt intruded within the volcanic segments could be tapped into the Wonji fault plumbing systems (Rooney et al., 2007)

and erupt regionally (e.g., Nqub or Nquw), or alternatively could stall and fractionate, ultimately allowing evolved melts to accumulate in the upper crust. While studies from other rift zones and extensional-transtensional settings (e.g., Taupo Volcanic Zone, Spinks et al., 2005, and the Altiplano-Puna Plateau in the Central Andes, Acocella et al., 2011) have demonstrated strong correlations between extension rate, magma storage volumes and eruption rates the limited available age and volume controls on MER volcanism currently hamper similar rift-scale comparisons and our understanding of the tectonomagmatic processes that generated the silicic magma systems. It has, however, been suggested that the silicic volcanoes of the MER are located at the ends of the volcanic segments (e.g., Mohr et al., 1980; Casey et al., 2006) and it is commonly assumed that complex extensional stress field (Keranen et al., 2004) and/or the cooled crust abutting the segment tip (Ebinger et al., 2008) hindered magma ascent at these sites. An alternative view is that once the upper crustal reservoir and the volcanic edifice began to establish then the stress regime could have acted to focus magma ascent in the crust, essentially capturing later melts beneath the volcanic edifice (Karlstrom et al., 2009). In any case we suggest that the evolved silicic melts of Aluto represent the stalled, structurally focused component of mantle-derived basaltic melts. Further structural and geochronological investigations will be vital for understanding the links between tectonics and the rise and emplacement of magma across and along the MER.

The earliest silicic eruptions from Aluto were trachytic (Qdt, Fig. 13C), and it is plausible that the peralkaline melts that would later form the major ignimbrites (Qgyi and Qgei) were extracted from the trachytes (e.g., Rooney et al., 2012). Incompatible trace elements and modelling (Figs. 11 and 12) indicate that trachytic lava can be produced via ~70% fractional crystallization from the least evolved (parental) basaltic lavas found in the study area, while welded ignimbrites require >80% fractionation.

The large silicic melt reservoir (pre-requisite for units Qgei and Qgyi) was likely to have been assembled during an episode of high heat and mass input (e.g., Tappa et al., 2011; Frazer et al., 2014; Macdonald et al., 2014). The elevated rates of magma and heat supply may have limited the degree of differentiation, and hence incompatible element concentrations in the pre- and syn-caldera samples (e.g., Y, Nb, La, Rb and Zr, Fig. 11) do no approach the high values seen in many of the recent post-caldera products. A similar temporal trend is observed at Longonot (Macdonald et al., 2014) where periods of strong convection in the magma reservoir in the build up to caldera formation limit any extreme compositional variations. By ~310 ka a large volume of melt- and volatile-rich magma had formed at shallow crustal levels beneath Aluto and the major caldera-forming eruptions could be initiated (Fig. 13D). The substantial time gap of ~250 ka between the welded ignimbrites and post-caldera phases (Fig. 13 E, Section 7.5) suggests that there was a substantial withdrawal of eruptible magma from the upper crustal chamber.

The first post-caldera phase of Aluto (comenditic rhyolites, Qcr) are less evolved than the major welded ignimbrite units and fall off the fractionation trend for certain trace elements (e.g., La and Y in Fig. 11). It is has been demonstrated at a number of other peralkaline systems that the first post-caldera phases consist of mixed rhyolites and trachytes with mafic material from lower in the reservoir (e.g., at Menegai, Leat et al., 1984 and Longonot, Macdonald et al., 2014). While the data presented here do not allow us to thoroughly address this issue we suggest that dedicated microanalytical and isotopic studies of the comenditic rhyolites (Qcr) will be key to identifying evidence for melt mixing and contamination.

The post-caldera rhyolites display a large range of incompatible element concentrations and the pumice unit Qup, which likely represents a Plinian eruption, has the most chemically evolved composition (Fig. 11). The extreme enrichments in incompatible element concentrations after ~60 ka may be explained by formation of a stratified shallow magmatic reservoir with a compositionally zoned cap (e.g., Mahood, 1981; Leat et al., 1984; Mahood and Hildreth, 1986; Civetta et al., 1988; Macdonald and Scaillet, 2006; Neave et al., 2012; Macdonald et al., 2014). In this case the most evolved compositions (e.g., Qup) would be generated following periods of extensive crystal fractionation and/or decreasing melt supply to the shallow magmatic reservoir, which would have driven the magma in the cap to more evolved compositions.

Intermediate lavas (Qwai) are demonstrably scarce (Fig. 4) but yield valuable insights into current state of magmatic system. Intermediate eruptions are restricted to low-lying vents in faulted regions west of the edifice (Section 5.2.2) and the presence of silicic enclaves within the scoria cone sequences (Section 6.1) suggest that mafic and silicic compositions must be present within the same magma plumbing system. On the main edifice of Aluto there is no evidence for mafic-intermediate magmas having erupted, nor do we find any mixing-mingling between mafic-intermediate and silicic magmas. Peralkaline melt zones are commonly assumed to form a density barrier that prohibits mafic melts from reaching the surface (Mahood, 1984; Neave et al., 2012). The fact that no mafic-intermediate lavas are found on the centre of the Aluto edifice suggests that peralkaline melts beneath the complex are sufficiently aggregated to prohibit ascent of dense mafic melts. Hence the rise of mafic-intermediate magma to the surface can only be accomplished via fault networks beyond the edge of the silicic melt cap. This contrasts markedly with Gedemsa (a peralkaline complex 75 km north-east of Aluto) where basaltic lavas have erupted within the caldera and have entrained silicic liquids as well as partially crystalline silicic rock fragments (Peccerillo et al., 2003). Aluto has undergone much greater volumes of post-caldera volcanism than Gedemsa (Hutchison et al., in press) it also hosts a much larger geothermal field and shows current evidence for ground deformation (Biggs et al., 2011; Hutchison et al., 2016), these lines of evidence as well as the absence of mafic lavas on the centre of the complex are consistent with a more consolidated melt zone at Aluto.

8.2. The pace of silicic volcanism in the MER

Our stratigraphy shows that Aluto underwent an early phase of edifice building (duration not yet constrained but likely on order of 150–400 ka, based on similar peralkaline complexes in the Kenyan rift, e.g., Menegai, Leat et al., 1984 and Longonot, Clarke et al., 1990), major ignimbrite eruptions at ~310 ka, a period of repose lasting 250 ka and then episodic post-caldera volcanism after ~60 ka. The apparent lack of volcanic activity at Aluto between 300 and 60 ka could be explained by a real hiatus in volcanism, or potentially a gap in sampling. Our updated stratigraphy (Fig. 3) represents the most complete coverage of the volcanic eruptive events to date, and on the basis of our lithological correlations between the surface and deep stratigraphy (Section 5.3) we consider that this hiatus in volcanism is real. However, until unambiguous geochronological measurements are made across a complete field or core section that covers the transition from major ignimbrite eruptions to the post-caldera eruptions some uncertainty remains.

Overall, our geological interpretations and new ages suggest that silicic volcanism at Aluto can be considered episodic on a variety of timescales. Large volume caldera-forming events take place on long-timescales >100 ka, linked to substantial deliveries of mantle-derived melt to the mid-crust. Stalling of magmas and melt capture processes (e.g., Keranen et al., 2004; Ebinger et al., 2008; Karlstrom et al., 2009) help to assemble large volume upper-crustal magma reservoirs (>10 km^3), and crystal fractionation is key to driving melt evolution to silicic compositions (Peccerillo et al., 2003; Rooney et al., 2012). We also see evidence for shorter timescale (ca. 10 ka) eruptive cycles, represented at Aluto by unconformity-bounded post-caldera phases (Fig. 3, Section 7.5). These cycles may link to the recharge and replenishment of small volumes (<10 km^3) of melt and volatiles in the cap of established upper crustal reservoirs (e.g., Civetta et al., 1988).

Table 3
Potential volcanic hazards at Aluto. Population data was provided by the Smithsonian Global Volcanism Program (Siebert and Simkin, 2002).

Potential hazard	Eruption of tephra	Phreatomagmatic/ Phreatic eruptions	Pyroclastic density current (PDC)	Lava flow (basaltic)	Lava dome (rhyolitic)	Changes in diffuse degassing	Debris avalanche
Origin and characteristics	Explosive vertical eruption of pumice and lithic fragments into the air; distribution controlled by column height and wind field	Magma water interaction, explosion due to rapid release of steam; vent will be located within geothermal field	Eruption of molten/hot fragments of pumice entraining lithic clasts; distribution is topographically controlled	Largely effusive eruption of molten lava, slow moving, controlled by topography	Initiate with explosive eruption building up pumice dome near vent; rhyolite lava breaches dome and is emplaced slowly and will be topographically controlled	Areas of diffuse degassing migrate with time; potential for dense volcanic gases (e.g., CO_2) to concentrate in depressions	Result from slope failure of volcanic edifice
Typical length scale (relative to vent)	10–30 km	5 km	10 km	500 m to 1 km	500 m to 2.5 km	1 km	<5 km
Effect on land and objects	Blanketing of land and loading of property near vent	Burning, burial and impact damage to land and property	Burning, burial and impact damage to land and property	Burning, burial and destruction of land and property	Burning, burial and destruction of land and property	Destruction and damage to vegetation; danger for people living in properties nearby where gases (e.g., CO_2) can accumulate	Burial and destruction of land and property
Degree of risk and population exposure	Moderate for people living within 10 km of volcano (25,000); low to people beyond this (315,000)	High for people living within 5 km of volcano (6000), low for people within 10 km (25,000)	High for people living within 10 km of volcano (25,000), particularly those closest to volcano and living in valleys	Low for people living within 10 km of volcano (25,000), typically associated with fault zones on flanks of complex	Low to moderate for people living within 10 km of volcano (25,000), explosive phases and dome collapse represent greatest risk	Low for people living with 5 km of volcano (6000)	High for people living with 5 km of volcano (6000), especially for those living adjacent to steep slopes at the base of complex
Number of deposits recognized in last 10,000 years	At least one eruption in last 10,000 years emplaced tephra to >10 km from vent, pumice fall on main edifice is 2–3 m thick	unknown	At least one PDC deposit within caldera following Qup unit (Fig. 5E, F), deposits are 5–10 m thick on main edifice	At least one basaltic eruption. Qwai lava flow deposit 2.5 km west of Adami Tullo (Qwai, Fig. 4) appears fresh, no cover by Qup	Approximately thirteen silicic domes within the last 10,000 years, some may have erupted synchronously, suggest eruption rate of around 1 per 1000 years. Volume typically between 1 and 100 km^3, with maximum of ~250 km^3	unknown	unknown

8.3. Future volcanic hazards

Volcanic phenomena that have occurred at Aluto in the last 10 ka include obsidian coulees (Qpoy), pumice cones and PDCs (Qpby), and pumice fallout (Qup). Lahars (Qal) have also occurred, although may only have been facilitated during episodes of humid climate prior to ~5 ka (e.g., Le Turdu et al., 1999; Benvenuti et al., 2002). In Table 3 we evaluate potential volcanic hazards and population exposure at Aluto.

Based on the record of recent volcanism, a future eruption of Aluto will likely begin with a moderate explosive eruption to form a pumice cone (potentially with localized PDCs), followed by emplacement of an obsidian coulee (Table 3). The recent obsidian coulees (Qpoy) have volumes of 1–100 $\times 10^6$ m^3 (e.g., Fig. S1A). Pumice cones (Qpby) built up prior to the obsidian coulees are difficult to trace laterally, but we estimate that small cones have volumes of ~10×10^6 m^3 while the largest pumice cones (e.g., the large Qpby dome mapped north of well LA-6, Fig. 4) have volumes of ~250×10^6 m^3. Our geological mapping (Fig. 4) shows that there have been thirteen obsidian coulees (map unit Qpoy) emplaced over the last ~10,000 years (assuming radiocarbon age correlations for Qup are valid, Section 5.3). Of the thirteen Qpoy coulees that have erupted a few of these appear to have erupted synchronously, and for simplicity, if we assume there have been 10 distinct eruptions, this would support an average silicic lava dome eruption at a rate of 1 per 1000 years. This value is broadly in line with observations of tephra layers preserved in lacustrine sections west of the Aluto that showed ~13 tephra horizons within the Abernosa pumice deposit, which spans a period of ~15,000 years (Section 5.3, Gasse and Street, 1978).

Radiocarbon ages demonstrate that volcanism has occurred relatively recently at Aluto (~0.4 cal. ka BP, Hutchison et al., in press) and a salient feature of this current phase of activity is that lavas have erupted from discrete vents associated with volcanic and tectonic faults (Hutchison et al., 2015) but they show no obvious spatial progression with time. Dedicated volcanic monitoring is an important next step and remote sensing methods (e.g., InSAR, Biggs et al., 2011) have the potential to be vital for constraining magma movement within the subsurface prior to future eruptions. Expansion of geothermal infrastructure across these silicic volcanoes offers an opportunity to build permanent monitoring networks (e.g., seismic and continuous GPS stations) to assess volcanic hazards and monitor geothermal resources at these new installations. More generally, a thorough understanding of the recurrence interval of post-caldera phases (e.g., Pyle and Elliott, 2006; Nomikou et al., 2014), detailed mapping of tephra fall (e.g., Fontijn et al., 2010, 2011) and PDC deposits (e.g., Wiart and Oppenheimer, 2000, 2005; Rampey et al., 2010, 2014), and forward modelling of a spectrum of eruption scenarios (e.g. Aspinall and Woo, 2014; Jenkins et al., 2015) will be critical for developing probabilistic models of volcanic hazard at Aluto.

9. Conclusions

Field mapping, remote sensing, geochronology and geochemistry provide new insights into the eruptive history and magmatic evolution

of the Aluto volcanic complex in Ethiopia. The first eruptions followed a period of mafic fissure volcanism and rift basin development. The complex was initially built up as a trachytic edifice, via both explosive and effusive activity. At ~310 ka the complex underwent a phase of major explosive activity (represented in the field by extensive welded ignimbrite sheets) which we propose developed a caldera rim structure and ring fault. After a substantial hiatus in activity, post-caldera volcanism began at ~60 ka. We identify four distinct post-caldera rhyolitic sequences that include pumice fall, PDC and lava flow units. These sequences have progressively in-filled the caldera and their vents are frequently aligned along pre-existing structural weaknesses of both volcanic and tectonic origin. Whole-rock geochemical data suggests that crustal melting did not play a significant role in generating the evolved rocks of Aluto, and without isotopic constraints the simplest interpretation of our data is that silicic magmas of Aluto were mainly generated through protracted fractional crystallization processes. Recent silicic eruptions appear to occur at an average rate of 1 per 1000 years, and we expect that future eruptions of Aluto will involve explosive emplacement of localised pumice cones and effusive obsidian coulees of volumes between 1 and 100 $\times$ 10^6 m^3. Given that >300,000 people live within 30 km of Aluto, as well as the targeted geothermal investment, dedicated monitoring via remote sensing and/or field installations is a critical next step to enable effective management and mitigation of future risk at this volcano.

Supplementary data to this article can be found online at http://dx.doi.org/10.1016/j.jvolgeores.2016.09.010.

Acknowledgments

This work is a contribution to the NERC funded RiftVolc project (NE/L013932/1, Rift volcanism: past, present and future). Airborne data used for geological mapping was collected by NERC ARSF (flight ET12-17-321). N. Marsh and R. Kelly (University of Leicester) provided assistance with XRF, S. Wyatt, P. Holdship and K. Fontijin (University of Oxford) supported the ICP-MS. $^{40}Ar/^{39}Ar$ analysis at SUERC was generously supported by a NERC Argon Isotope Facility grant (IP-1506-1114). Technical assistance at SUERC was provided by R. Dymock and J. Imlach. Field assistance was provided by T. Bedada, A. Zafu, F. Aduna, E. Robertson, M. Hutchinson and G. Andarge. The Geological Survey of Ethiopia provided access to archived data and drilling reports from Aluto. The Ethiopian Electric Power Company provided logistical support throughout the field campaign. W.H., D.M.P., T.A.M. and J.B. are supported by and contribute to the NERC Centre for the Observation and Modelling of Earthquakes, Volcanoes and Tectonics (COMET). W.H. was funded by NERC studentship, NE/J5000045/1. Additional funding for the project was provided by: University College and the Department of Zoology (Boise Trust Fund) at the University of Oxford, as well as the Geological Remote Sensing Group, the Edinburgh Geological Society and the Leverhulme Trust. V. Acocella and anonymous reviewer provided valuable comments that helped improve the original manuscript. The research materials supporting this publication can be accessed from http://dx.doi.org/10.6084/m9.figshare.1261646.

References

Abebe, B., Acocella, V., Korme, T., Ayalew, D., 2007. Quaternary faulting and volcanism in the Main Ethiopian Rift. J. Afr. Earth Sci. 48:115–124. http://dx.doi.org/10.1016/j.jafrearsci.2006.10.005.

Acocella, V., Korme, T., Salvini, F., Funiciello, R., 2002. Elliptic calderas in the Ethiopian Rift : control of pre-existing structures. J. Volcanol. Geotherm. Res. 119, 189–203.

Acocella, V., Gioncada, A., Omarini, R., Riller, U., Mazzuoli, R., Vezzoli, L., 2011. Tectonomagmatic characteristics of the back-arc portion of the Calama–Olacapato–El Toro Fault Zone, Central Andes. Tectonics 30, TC3005. http://dx.doi.org/10.1029/2010TC002854.

Agostini, A., Bonini, M., Corti, G., Sani, F., Mazzarini, F., 2011. Fault architecture in the Main Ethiopian Rift and comparison with experimental models: Implications for rift evolution and Nubia–Somalia kinematics. Earth Planet. Sci. Lett. 301:479–492. http://dx.doi.org/10.1016/j.epsl.2010.11.024.

Aspinall, W.P., Woo, G., 2014. Santorini unrest 2011–2012: an immediate Bayesian belief network analysis of eruption scenario probabilities for urgent decision support under uncertainty. J. Appl. Volcanol. 3, 1–12.

Aspinall, W., Auker, M., Hincks, T., Mahony, S., Nadim, F., Pooley, J., Sparks, R.S.J., Syre, E., 2011. Volcano hazard and exposure in GFDRR priority countries and risk mitigation measures. Volcano Risk Study 0100806–00-1-R. Global Facility for Disaster Reduction and Recovery, Washington, D. C.

Barberi, F., Ferrara, G., Santacroce, R., Treuil, M., Varet, J., 1975. A transitional basalt-pantellerite sequence of fractional crystallization, the Boina Centre (Afar Rift, Ethiopia). J. Petrol. 16:22–56. http://dx.doi.org/10.1093/petrology/16.1.22.

Bendick, R., McClusky, S., Bilham, R., Asfaw, L., Klemperer, S., 2006. Distributed Nubia–Somalia relative motion and dike intrusion in the Main Ethiopian Rift. Geophys. J. Int. 165, 303–310.

Benito-Calvo, A., Barfod, D.N., McHenry, L.J., de la Torre, I., 2014. The geology and chronology of the Acheulean deposits in the Mieso area (East-Central Ethiopia). J. Hum. Evol. 76, 26–38.

Benvenuti, M., Carnicelli, S., Belluomini, G., Dainelli, N., Di Grazia, S., Ferrari, G., Iasio, C., Sagri, M., Ventra, D., Atnafu, B., 2002. The Ziway–Shala lake basin (main Ethiopian rift, Ethiopia): a revision of basin evolution with special reference to the Late Quaternary. J. Afr. Earth Sci. 35:247–269. http://dx.doi.org/10.1016/S0899-5362(02)00036-2.

Benvenuti, M., Bonini, M., Tassi, F., Corti, G., Sani, F., Agostini, A., Manetti, P., Vaselli, O., 2013. Holocene lacustrine fluctuations and deep CO2 degassing in the northeastern Lake Langano Basin (Main Ethiopian Rift). J. Afr. Earth Sci. 77:1–10. http://dx.doi.org/10.1016/j.jafrearsci.2012.09.001.

Beutel, E., van Wijk, J., Ebinger, C., Keir, D., Agostini, A., 2010. Formation and stability of magmatic segments in the Main Ethiopian and Afar rifts. Earth Planet. Sci. Lett. 293:225–235. http://dx.doi.org/10.1016/j.epsl.2010.02.006.

Biggs, J., Bastow, I.D., Keir, D., Lewi, E., 2011. Pulses of deformation reveal frequently recurring shallow magmatic activity beneath the Main Ethiopian Rift. Geochem. Geophys. Geosyst. 12:1–11. http://dx.doi.org/10.1029/2011GC003662.

Black, S., Macdonald, R., Kelly, M.R., 1997. Crustal origin for peralkaline rhyolites from Kenya: evidence from U-series disequilibria and Th-isotopes. J. Petrol. 38, 277–297.

Blundy, J.D., Wood, B.J., 1991. Crystal-chemical controls on the partitioning of Sr and Ba between plagioclase feldspar, silicate melts, and hydrothermal solutions. Geochim. Cosmochim. Acta 55:193–209. http://dx.doi.org/10.1016/0016-7037(91)90411-W.

Boccaletti, M., Bonini, M., Mazzuoli, R., Abebe, B., 1998. Quaternary oblique extensional tectonics in the Ethiopian Rift (Horn of Africa). Tectonophysics 287, 97–116.

Bohrson, W.A., Reid, M.R., 1997. Genesis of silicic peralkaline volcanic rocks in an ocean island setting by crustal melting and open-system processes: Socorro Island, Mexico. J. Petrol. 38, 1137–1166.

Bonini, M., Corti, G., Fabrizio, I., Manetti, P., Mazzarini, F., Abebe, T., Pecskay, Z., 2005. Evolution of the Main Ethiopian Rift in the frame of Afar and Kenya rifts propagation. Tectonics 24. http://dx.doi.org/10.1029/2004TC001680.

Brown, S.K., Sparks, R.S.J., Ilyinskaya, E., Jenkins, S., Loughlin, S.C., Mee, K., Vye-Brown, C., et al., 2015. Regional and country profiles of volcanic hazard and risk. Report IV of the GVM/IAVCEI contribution to the Global Assessment Report on Disaster Risk Reduction 2015. Global Volcano Model and IAVCEI.

Caricchi, L., Ulmer, P., Peccerillo, A., 2006. A high-pressure experimental study on the evolution of the silicic magmatism of the Main Ethiopian Rift. Lithos 91:46–58. http://dx.doi.org/10.1016/j.lithos.2006.03.008.

Casey, M., Ebinger, C., Keir, D., Gloaguen, R., Mohamed, F., 2006. Strain accommodation in transitional rifts : extension by magma intrusion and faulting in Ethiopian rift magmatic segments. In: Yirgu, G., Ebinger, C.J., Maguire, P.K.H. (Eds.), The Afar Volcanic Province within the East African Rift System. Geological Society, London, Special Publications, pp. 143–163.

Central Statistical Agency [Ethiopia] and ICF International, 2012. Ethiopia Demographic and Health Survey 2011. Central Statistical Agency and ICF International, Addis Ababa, Ethiopia and Calverton, Maryland, USA.

Civetta, L., Cornette, Y., Gillot, P.Y., Orsi, G., 1988. The eruptive history of Pantelleria (Sicily Channel) in the last 50 ka. Bull. Volcanol. 50, 47–57.

Civetta, L., D'Antonio, M., Orsi, G., Tilton, G.R., 1998. The Geochemistry of Volcanic Rocks from Pantelleria Island, Sicily Channel: Petrogenesis and Characteristics of the Mantle Source Region. J. Petrol. 39:1453–1491. http://dx.doi.org/10.1093/petroj/39.8.1453.

Clarke, M.G.C., Woodhall, D., Allen, G., Darling, W.G., 1990. Geological, Volcanological and Hydrogeological Controls on the Occurrence of Geothermal Activity in the Area Surrounding Lake Naivasha, Kenya. British Geological Survey. Derry and Sons Ltd., Nottingham (ed.).

Cornwell, D.G., Maguire, P.K.H., England, R.W., Stuart, G.W., 2010. Imaging detailed crustal structure and magmatic intrusion across the Ethiopian Rift using a dense linear broadband array. Geochem. Geophys. Geosyst. 11.

Corti, G., 2009. Continental rift evolution: From rift initiation to incipient break-up in the Main Ethiopian Rift, East Africa. Earth Sci. Rev. 96:1–53. http://dx.doi.org/10.1016/j.earscirev.2009.06.005.

Corti, G., Philippon, M., Sani, F., Keir, D., Kidane, T., 2013. Re-orientation of the extension direction and pure extensional faulting at oblique rift margins: Comparison between the Main Ethiopian Rift and laboratory experiments. Terra Nova 25:396–404. http://dx.doi.org/10.1111/ter.12049.

Dakin, G., Gibson, I.L., 1971. A Preliminary Account of Alutu, a Pantelleritic Volcano in the Main Ethiopian Rift. Bull. Geophys. Obs. Addis Ababa 13, 110–114.

Davies, G.R., Macdonald, R., 1987. Crustal Influences in the Petrogenesis of the Naivasha Basalt—Comendite Complex: Combined Trace Element and Sr-Nd-Pb Isotope Constraints. J. Petrol. 28, 1009–1031.

Di Paola, G.M., 1972. The Ethiopian Rift Valley (between 7° 00′ and 8° 40′ lat. North). Bull. Volcanol. 36:517–560. http://dx.doi.org/10.1007/BF02599823.

Ebinger, C., 2005. Continental break-up: the East African perspective. Astron. Geophys. 46, 16–21.
Ebinger, C.J., Casey, M., 2001. Continental breakup in magmatic provinces: An Ethiopian example. Geology 29:527–530. http://dx.doi.org/10.1130/0091-7613(2001)029<0527:CBIMPA>2.0.CO;2.
Ebinger, C.J., Keir, D., Ayele, A., Calais, E., Wright, T.J., Belachew, M., Hammond, J.O.S., Campbell, E., Buck, W.R., 2008. Capturing magma intrusion and faulting processes during continental rupture: seismicity of the Dabbahu (Afar) rift. Geophys. J. Int. 174:1138–1152. http://dx.doi.org/10.1111/j.1365-246X.2008.03877.x.
ELC Electroconsult, 1986. Exploitation of Langano-Aluto geothermal resources feasibility report. Geothermal Exploration Project, Ethiopian Lake District Rift.
Ferguson, D.J., Barnie, T.D., Pyle, D.M., Oppenheimer, C., Yirgu, G., Lewi, E., Kidane, T., Carn, S., Hamling, I., 2010. Recent rift-related volcanism in Afar, Ethiopia. Earth Planet. Sci. Lett. 292:409–418. http://dx.doi.org/10.1016/j.epsl.2010.02.010.
Field, L., Blundy, J., Calvert, A., Yirgu, G., 2013. Magmatic history of Dabbahu, a composite volcano in the Afar Rift, Ethiopia. Geol. Soc. Am. Bull. 125, 128–147.
Field, L., Blundy, J., Brooker, R.A., Wright, T.Yirgu, 2012. Magma storage conditions beneath Dabbahu Volcano (Ethiopia) constrained by petrology, seismicity and satellite geodesy. Bull. Volcanol. 74 (5), 981–1004.
Fink, J., 1980. Surface folding and viscosity of rhyolite flows. Geology 8, 250–254.
Fontijn, K., Ernst, G.G.J., Elburg, M.A., Williamson, D., Abdallah, E., Kwelwa, S., Mbede, E., Jacobs, P., 2010. Holocene explosive eruptions in the Rungwe Volcanic Province, Tanzania. J. Volcanol. Geotherm. Res. 196:91–110. http://dx.doi.org/10.1016/j.jvolgeores.2010.07.021.
Fontijn, K., Ernst, G.G.J., Bonadonna, C., Elburg, M.A., Mbede, E., Jacobs, P., 2011. The ~4-ka Rungwe Pumice (South-Western Tanzania): A wind-still Plinian eruption. Bull. Volcanol. 73:1353–1368. http://dx.doi.org/10.1007/s00445-011-0486-8.
Fontijn, K., Elburg, M.A., Nikogosian, I.K., van Bergen, M.J., Ernst, G.G.J., 2013. Petrology and geochemistry of Late Holocene felsic magmas from Rungwe volcano (Tanzania), with implications for trachytic Rungwe Pumice eruption dynamics. Lithos 177:34–53. http://dx.doi.org/10.1016/j.lithos.2013.05.012.
Frazer, R.E., Coleman, D.S., Mills, R.D., 2014. Zircon U-Pb geochronology of the Mount Givens Granodiorite: Implications for the genesis of large volumes of eruptible magma. J. Geophys. Res. Solid Earth:2907–2924 http://dx.doi.org/10.1002/2013JB010716.
Gasse, E., Street, F., 1978. Late Quaternary lake-level fluctuations and environments of the northern Rift Valley and Afar region (Ethiopia and Djibouti). Palaeogeogr. Palaeoclimatol. Palaeoecol. 24.
Gebregzabher, Z., 1986. Hydrothermal alteration minerals in Aluto Langano geothermal wells, Ethiopia. Geothermics 15, 735–740.
Gianelli, G., Teklemariam, M., 1993. Water-rock interaction processes in the Aluto-Langano geothermal field (Ethiopia). J. Volcanol. Geotherm. Res. 56, 429–445.
Gibert, E., Travi, Y., Massault, M., Tiercelin, J.-J., Chernet, T., 2002. AMS-14C chronology of a lacustrine sequence from Lake Langano (Main Ethiopian Rift); correction and validation steps in relation with volcanism, lake water and carbon. Radiocarbon 44, 75–92.
Gibson, I.L., 1969. The structure and volcanic geology of an axial portion of the Main Ethiopian Rift. Tectonophysics http://dx.doi.org/10.1016/0040-1951(69)90054-7.
Gibson, I.L., 1970. A pantelleritic welded ash-flow tuff from the Ethiopian Rift Valley. Contrib. Mineral. Petrol. 28, 89–111.
Giordano, F., D'Antonio, M., Civetta, L., Tonarini, S., Orsi, G., Ayalew, D., Yirgu, G., Dell'Erba, F., Di Vito, M.A., Isaia, R., 2014. Genesis and evolution of mafic and felsic magmas at Quaternary volcanoes within the Main Ethiopian Rift: Insights from Gedemsa and Fanta 'Ale complexes. Lithos 188:130–144. http://dx.doi.org/10.1016/j.lithos.2013.08.008.
Gizaw, B., 1993. Aluto-Langano geothermal field, Ethiopian Rift Valley: physical characteristics and the effects of gas on well performance. Geothermics 22, 101–116.
Hayward, N., Ebinger, C., 1996. Variations in the along-axis segmentation of the Afar Rift system. Tectonics 15, 244–257.
Hutchison, W., Mather, T.A., Pyle, D.M., Biggs, J., Yirgu, G., 2015. Structural controls on fluid pathways in an active rift system: A case study of the Aluto volcanic complex. Geosphere:1–21 http://dx.doi.org/10.1130/GES01119.1.
Hutchison, W., Biggs, J., Mather, T.A., Pyle, Lewi, E., Yirgu, G., Caliro, S., Chiodini, G., Clor, L.E., Fischer, T.P., 2016. Causes of unrest at silicic calderas in the East African Rift: New constraints from InSAR and soil-gas chemistry at Aluto volcano, Ethiopia. Geochem. Geophys. Geosyst. 17. http://dx.doi.org/10.1002/2016GC006395.
Hutchison, W., Fusillo, R., Pyle, D.M., Mather, T.A., Blundy, J., Biggs, J., Yirgu, G., Cohen, B.E., Brooker, R., Barfod, D.N., Calvert, A.T., 2016. A pulse of mid-Pleistocene rift volcanism in Ethiopia at the dawn of modern humans. Nat. Commun. 7, 13192. http://dx.doi.org/10.1038/ncomms13192.
Irvine, T.N., Baragar, W.R.A., 1971. A guide to the chemical classification of the common volcanic rocks. Can. J. Earth Sci. 8, 523–548.
Jenkins, S.F., Barsotti, S., Hincks, T.K., Neri, A., Phillips, J.C., Sparks, R.S.J., Sheldrake, T., Vougioukalakis, G., 2015. Rapid emergency assessment of ash and gas hazard for future eruptions at Santorini Volcano, Greece. J. Appl. Volcanol. 4, 16.
Karlstrom, L., Dufek, J., Manga, M., 2009. Organization of volcanic plumbing through magmatic lensing by magma chambers and volcanic loads. J. Geophys. Res. Solid Earth 114:1–16. http://dx.doi.org/10.1029/2009JB006339.
Kebede, S., Mamo, T., Abebe, T., 1985. Geological report and explanation to the geological map of Aluto-Langano geothermal area. Ethiopian Institute of Geological Surveys, Addis Ababa (60 pp.).
Keir, D., Ebinger, C.J., Stuart, G.W., Daly, E., Ayele, A., 2006. Strain accommodation by magmatism and faulting as rifting proceeds to breakup: Seismicity of the northern Ethiopian rift. J. Geophys. Res. 111:1–17. http://dx.doi.org/10.1029/2005JB003748.
Keir, D., Bastow, I.D., Corti, G., Mazzarini, F., Rooney, T.O., 2015. The origin of along-rift variations in faulting and magmatism in the Ethiopian Rift. Tectonics 34:464–477. http://dx.doi.org/10.1002/2014TC003698.
Keranen, K., Klemperer, S.L., 2008. Discontinuous and diachronous evolution of the Main Ethiopian Rift: Implications for development of continental rifts. Earth Planet. Sci. Lett. 265:96–111. http://dx.doi.org/10.1016/j.epsl.2007.09.038.
Keranen, K., Klemperer, S.L., Gloaguen, R., 2004. Three-dimensional seismic imaging of a protoridge axis in the Main Ethiopian rift. Geology 32:949. http://dx.doi.org/10.1130/G20737.1.
Lahitte, P., Gillot, P.-Y., Courtillot, V., 2003. Silicic central volcanoes as precursors to rift propagation: the Afar case. Earth Planet. Sci. Lett. 207:103–116. http://dx.doi.org/10.1016/S0012-821X(02)01130-5.
Laury, R.L., Albritton, C.C., 1975. Geology of Middle Stone Age archaeological sites in the main Ethiopian rift valley. Geol. Soc. Am. Bull. 86:999–1011. http://dx.doi.org/10.1130/0016-7606(1975)86<999.
Le Maitre, R.W., Streckeisen, A., Zanettin, B., Le Bas, M.J., Bonin, B., Bateman, P., 2002. Igneous rocks: a classification and glossary of terms: recommendations of the International Union of Geological Sciences Subcommission on the Systematics of Igneous Rocks. Cambridge University Press.
Le Turdu, C., Tiercelin, J.-J., Gibert, E., Travi, Y., Lezzar, K.-E., Richert, J.-P., Massault, M., Gasse, F., Bonnefille, R., Decobert, M., Gensous, B., Jeudy, V., Tamrat, E., Mohammed, M.U., Martens, K., Atnafu, B., Chernet, T., Williamson, D., Taieb, M., 1999. The Ziway–Shala lake basin system, Main Ethiopian Rift: Influence of volcanism, tectonics, and climatic forcing on basin formation and sedimentation. Palaeogeogr. Palaeoclimatol. Palaeoecol. 150:135–177. http://dx.doi.org/10.1016/S0031-0182(98)00220-X.
Leat, P.T., MacDonald, R., Smith, R.L., 1984. Geochemical evolution of the Menengai Caldera Volcano, Kenya. J. Geophys. Res. Solid Earth 89:8571–8592. http://dx.doi.org/10.1029/JB089iB10p08571.
Lowenstern, J.B., Clynne, M.A., Bullen, T.D., 1997. Comagmatic A-type granophyre and rhyolite from the Alid volcanic center, Eritrea, northeast Africa. J. Petrol. 38, 1707–1721.
Maccaferri, F., Rivalta, E., Keir, D., Acocella, V., 2014. Off-rift volcanism in rift zones determined by crustal unloading. Nat. Geosci. 7, 297–300.
Macdonald, R., 1974. Nomenclature and petrochemistry of the peralkaline oversaturated extrusive rocks. Bull. Volcanol. 38, 498–516.
Macdonald, R., 2012. Evolution of peralkaline silicic complexes: Lessons from the extrusive rocks. Lithos 152, 11–22.
Macdonald, R., Scaillet, B., 2006. The central Kenya peralkaline province: Insights into the evolution of peralkaline salic magmas. Lithos 91:59–73. http://dx.doi.org/10.1016/j.lithos.2006.03.009.
Macdonald, R., Navarro, J.M., Upton, B.G.J., Davies, G.R., 1994. Strong compositional zonation in peralkaline magma: Menengai, Kenya Rift Valley. J. Volcanol. Geotherm. Res. 60:301–325. http://dx.doi.org/10.1016/0377-0273(94)90057-4.
Macdonald, R., Belkin, H.E., Fitton, J.G., Rogers, N.W., Nejbert, K., Tindle, A.G., Marshall, A.S., 2008. The Roles of Fractional Crystallization, Magma Mixing, Crystal Mush Remobilization and Volatile-Melt Interactions in the Genesis of a Young Basalt-Peralkaline Rhyolite Suite, the Greater Olkaria Volcanic Complex, Kenya Rift Valley. J. Petrol. 49: 1515–1547. http://dx.doi.org/10.1093/petrology/egn036.
Macdonald, R., Bagiński, B., Upton, B.G.J., 2014. The volcano–pluton interface; The Longonot (Kenya) and Kûngnât (Greenland) peralkaline complexes. Lithos 196, 232–241.
Mahood, G.A., 1981. Chemical evolution of a Pleistocene rhyolitic center: Sierra la Primavera, Jalisco, Mexico. Contrib. Mineral. Petrol. 77 (2), 129–149.
Mahood, G.A., 1984. Pyroclastic rocks and calderas associated with strongly peralkaline magmatism. J. Geophys. Res. 89:8540. http://dx.doi.org/10.1029/JB089iB10p08540.
Mahood, G.A., Hildreth, W., 1986. Geology of the peralkaline volcano at Pantelleria, Strait of Sicily. Bull. Volcanol. 48, 143–172.
Mamo, T., 1985. Petrography and rock chemistry of well LA-8 Aluto-Langano geothermal system, Ethiopia, Diploma report. Geothermal Institute, University of Auckland (48 pp.).
Ménard, C., Bon, F., Dessie, A., Bruxelles, L., Mensan, R., 2014. Late Stone Age variability in the Main Ethiopian Rift : New data from the Bulbula River, Ziway–Shala basin. Quat. Int. 343:53–68. http://dx.doi.org/10.1016/j.quaint.2014.07.019.
Mohr, P.A., 1971. Ethiopian rift and plateaus - Some volcanic petrochemical differences. 76:1967–1984. http://dx.doi.org/10.1029/JB076i008p01967.
Mohr, P.A., Potter, E.C., 1976. The Sagatu Ridge dike swarm, Ethiopian rift margin. J. Volcanol. Geotherm. Res.:55–71 http://dx.doi.org/10.1016/0377-0273(76)90018-4.
Mohr, P.A., Mitchell, J.G., Raynolds, R.G.H., 1980. Quaternary volcanism and faulting at O'A caldera, Central Ethiopian Rift. Bull. Volcanol. 43:173–189. http://dx.doi.org/10.1007/BF02597619.
Morgan, L.E., Renne, P.R., 2008. Diachronous dawn of Africa's Middle Stone Age: New $^{40}Ar/^{39}Ar$ ages from the Ethiopian Rift. Geology 36:967. http://dx.doi.org/10.1130/G25213A.1.
Mundula, F., Cioni, R., Mulas, M., 2013. Rheomorphic diapirs in densely welded ignimbrites: The Serra di Paringianu ignimbrite of Sardinia, Italy. J. Volcanol. Geotherm. Res. 258:12–23. http://dx.doi.org/10.1016/j.jvolgeores.2013.03.025.
Neave, D.a., Fabbro, G., Herd, R.a., Petrone, C.M., Edmonds, M., 2012. Melting, Differentiation and Degassing at the Pantelleria Volcano, Italy. J. Petrol. 53:637–663. http://dx.doi.org/10.1093/petrology/egr074.
Nomikou, P., Parks, M.M., Papanikolaou, D., Pyle, D.M., Mather, T.A., Carey, S., Watts, A.B., Paulatto, M., Kalnins, M.L., Livanos, I., Bejelou, K., Simou, E., Perros, I., 2014. The emergence and growth of a submarine volcano: The Kameni islands, Santorini (Greece). GeoResJ 1-2:8–18. http://dx.doi.org/10.1016/j.grj.2014.02.002.
Peccerillo, A., Mandefro, B., Solomon, G., Bedru, H., Tesfaye, K., 1998. The Precambrian rocks from Southern Ethiopia: petrology, geochemistry and their interaction with the recent volcanism from the Ethiopian Rift Valley. N. Jb. Mineral. 237–262.
Peccerillo, A., Barberio, M.R., Yirgu, G., Ayalew, D., Barbieri, M., Wu, T.W., 2003. Relationships between Mafic and Peralkaline Silicic Magmatism in Continental Rift Settings:

a Petrological, Geochemical and Isotopic Study of the Gedemsa Volcano, Central Ethiopian Rift. J. Petrol. 44:2003–2032. http://dx.doi.org/10.1093/petrology/egg068.
Peccerillo, A., Donati, C., Santo, A., Orlando, A., 2007. Petrogenesis of silicic peralkaline rocks in the Ethiopian rift: geochemical evidence and volcanological implications. J. Afr. Earth 48:161–173. http://dx.doi.org/10.1016/j.jafrearsci.2006.06.010.
Piperno, M., Collina, C., Gallotti, R., Raynal, J.-P., Kieffer, G., le Bourdonnec, F.-X., Poupeau, G., Geraads, D., 2009. Introduction: Current Issues in Oldowan Research. In: Braun, D.R., Hovers, E. (Eds.), Interdisciplinary Approaches to the Oldowan. Springer, Netherlands:pp. 111–128 http://dx.doi.org/10.1007/978-1-4020-9059-2.
Pizzi, A., Coltorti, M., Abebe, B., Disperati, L., Sacchi, G., Salvini, R., 2006. The Wonji fault belt (Main Ethiopian Rift): structural and geomorphological constraints and GPS monitoring. Geol. Soc. Lond. Spec. Publ. 259:191–207. http://dx.doi.org/10.1144/GSL.SP.2006.259.01.16.
Pyle, D.M., Elliott, J.R., 2006. Quantitative morphology, recent evolution, and future activity of the Kameni Islands volcano, Santorini, Greece. Geosphere 2:253. http://dx.doi.org/10.1130/GES00028.1.
Rampey, M.L., Oppenheimer, C., Pyle, D.M., Yirgu, G., 2010. Caldera-forming eruptions of the Quaternary Kone Volcanic Complex, Ethiopia. J. Afr. Earth Sci. 58:51–66. http://dx.doi.org/10.1016/j.jafrearsci.2010.01.008.
Rampey, M.L., Oppenheimer, C., Pyle, D.M., Yirgu, G., 2014. Journal of African Earth Sciences Physical volcanology of the Gubisa Formation, Kone Volcanic Complex, Ethiopia. J. Afr. Earth Sci. 96:212–219. http://dx.doi.org/10.1016/j.jafrearsci.2014.04.009.
Reimer, P.J., Bard, E., Bayliss, A., Beck, J.W., Blackwell, P.G., Bronk Ramsey, C., Buck, C.E., Cheng, H., Edwards, R.L., Friedrich, M., Grootes, P.M., Guilderson, T.P., Haflidason, H., Hajdas, I., Hatté, C., Heaton, T.J., Hoffmann, D.L., Hogg, A.G., Hughen, K.A., Kaiser, K.F., Kromer, B., Manning, S.W., Niu, M., Reimer, R.W., Richards, D.A., Scott, E.M., Southon, J.R., Staff, R.A., Turney, C.S.M., van der Plicht J., 2013. IntCal13 and Marine13 radiocarbon age calibration curves 0–50,000 years cal BP. Radiocarbon 55 (4), 1869–1887.
Ronga, F., Lustrino, M., Marzoli, A., Melluso, L., 2009. Petrogenesis of a basalt–comendite–pantellerite rock suite: the Boseti Volcanic Complex (Main Ethiopian Rift). Contrib. Mineral. Petrol. 98, 227–243.
Rooney, T., Furman, T., Bastow, I., Ayalew, D., Yirgu, G., 2007. Lithospheric modification during crustal extension in the Main Ethiopian Rift. J. Geophys. Res. 112. http://dx.doi.org/10.1029/2006JB004916.
Rooney, T.O., Hart, W.K., Hall, C.M., Ayalew, D., Ghiorso, M.S., Hidalgo, P., Yirgu, G., 2012. Peralkaline magma evolution and the tephra record in the Ethiopian Rift. Contrib. Mineral. Petrol. 164:407–426. http://dx.doi.org/10.1007/s00410-012-0744-6.
Sahle, Y., Hutchings, W.K., Braun, D.R., Sealy, J.C., Morgan, L.E., Negash, A., Atnafu, B., 2013. Earliest stone-tipped projectiles from the Ethiopian rift date to >279,000 years ago. PLoS One 8:1–9. http://dx.doi.org/10.1371/journal.pone.0078092.
Sahle, Y., Morgan, L.E., Braun, D.R., Atnafu, B., Hutchings, W.K., 2014. Chronological and behavioral contexts of the earliest Middle Stone Age in the Gademotta Formation, Main Ethiopian Rift. Quat. Int. 331:6–19. http://dx.doi.org/10.1016/j.quaint.2013.03.010.
Saibi, H., Aboud, E., Ehara, S., 2012. Analysis and interpretation of gravity data from the Aluto-Langano geothermal field of Ethiopia. Acta Geophys. 60:318–336. http://dx.doi.org/10.2478/s11600-011-0061-x.
Saria, E., Calais, E., Stamps, D.S., Delvaux, D., Hartnady, C.J.H., 2014. Present-day kinematics of the East African Rift. J. Geophys. Res. Solid Earth 119, 3584–3600.
Scott, S.C., 1980. The Geology of Longonot Volcano, Central Kenya: A Question of Volumes. Philos. Trans. R. Soc. A Math. Phys. Eng. Sci. http://dx.doi.org/10.1098/rsta.1980.0188.
Scott, S.C., Skilling, I.P., 1999. The role of tephrachronology in recognizing synchronous caldera-forming events at the Quaternary volcanoes Longonot and Suswa, south Kenya Rift. Geol. Soc. Lond. Spec. Publ. 161:47–67. http://dx.doi.org/10.1144/GSL.SP.1999.161.01.05.
Siebert, L., Simkin, T., 2002. Volcanoes of the World: an Illustrated Catalog of Holocene Volcanoes and their Eruptions. Smithsonian Institution, Global Volcanism Program Digital Information Series, GVP-3 (http://www.volcano.si.edu).
Sparks, R.S.J., Wilson, C.J.N., 1990. The Minoan deposits: a review of their characteristics and interpretation. In: Hardy, D., Keller, J., Galanopoulos, V.P., Flemming, N.C., Druitt, T.H. (Eds.), Thera and the Aegean World III. Thera Foundation London, London, pp. 89–99.
Spinks, K.D., Acocella, V., Cole, J.W., Bassett, K.N., 2005. Structural control of volcanism and caldera development in the transtensional Taupo Volcanic Zone, New Zealand. J. Volcanol. Geotherm. Res. 144, 7–22.
Street, F., 1979. Quaternary lakes in the Ziway–Shala Basin, Southern Ethiopia. Ph.D thesis. University of Cambridge.
Tappa, M.J., Coleman, D.S., Mills, R.D., Samperton, K.M., 2011. The plutonic record of a silicic ignimbrite from the Latir volcanic field, New Mexico. Geochem. Geophys. Geosyst. 12:1–16. http://dx.doi.org/10.1029/2011GC003700.
Teklemariam, M., 1996. Water-rock interaction processes in the Aluto-Langano geothermal field Ethiopia. Ph.D Thesis. University of Pisa (245 pp.).
Teklemariam, M., Battaglia, S., Gianelli, G., Ruggieri, G., 1996. Hydrothermal alteration in the Aluto-Langano geothermal field, Ethiopia. Geothermics 25, 679–702.
Trua, T., Deniel, C., Mazzuoli, R., 1999. Crustal control in the genesis of Plio-Quaternary bimodal magmatism of the Main Ethiopian Rift (MER): Geochemical and isotopic (Sr, Nd, Pb) evidence. Chem. Geol. 155:201–231. http://dx.doi.org/10.1016/S0009-2541(98)00174-0.
Valori, A.M., Teklemariam, M., Ginaelli, G., 1992. Evidence of temperature increase of CO_2-bearing fluids from Aluto-Langano geothermal field (Ethiopia): A fluid inclusions study of deep wells LA-3 and LA-6. Eur. J. Mineral. 4, 907–919.
Vogel, N., Nomade, S., Negash, A., Renne, P.R., 2006. Forensic $^{40}Ar/^{39}Ar$ dating: a provenance study of Middle Stone Age obsidian artifacts from Ethiopia. J. Archaeol. Sci. 33:1749–1765. http://dx.doi.org/10.1016/j.jas.2006.03.008.
Weaver, S.D., 1977. The Quaternary caldera volcano Emuruangogolak, Kenya Rift, and the petrology of a bimodal ferrobasalt-pantelleritic trachyte association. Bull. Volcanol. 40, 209–230.
White, J.C., Parker, D.F., Ren, M., 2009. The origin of trachyte and pantellerite from Pantelleria, Italy: Insights from major element, trace element, and thermodynamic modelling. J. Volcanol. Geotherm. Res. 179:33–55. http://dx.doi.org/10.1016/j.jvolgeores.2008.10.007.
Wiart, P., Oppenheimer, C., 2000. Largest known historical eruption in Africa: Dubbi volcano, Eritrea, 1861. Geology 28, 291–294.
Wiart, P., Oppenheimer, C., 2005. Large magnitude silicic volcanism in north Afar: The Nabro Volcanic Range and Ma'alalta volcano. Bull. Volcanol. 67:99–115. http://dx.doi.org/10.1007/s00445-004-0362-x.
Williams, F.M., Williams, M.A.J., Aumento, F., 2004. Tensional fissures and crustal extension rates in the northern part of the Main Ethiopian Rift. J. Afr. Earth Sci. 38:183–197. http://dx.doi.org/10.1016/j.jafrearsci.2003.10.007.
Williams, R., Branney, M.J., Barry, T.L., 2013. Temporal and spatial evolution of a waxing then waning catastrophic density current revealed by chemical mapping. Geology 42:107–110. http://dx.doi.org/10.1130/G34830.1.
Wilson, T.M., Stewart, C., Sword-Daniels, V., Leonard, G.S., Johnston, D.M., Cole, J.W., Wardman, J., Wilson, G., Barnard, S.T., 2012. Volcanic ash impacts on critical infrastructure. Phys. Chem. Earth A/B/C 45, 5–23.
Wilson, G., Wilson, T.M., Deligne, N.I., Cole, J.W., 2014. Volcanic hazard impacts to critical infrastructure: A review. J. Volcanol. Geotherm. Res. 286, 148–182.
WoldeGabriel, G., Aronson, J.L., Walter, R.C., 1990. Geology, geochronology, and rift basin development in the central sector of the Main Ethiopia Rift. Geol. Soc. Am. Bull. 102:439–458. http://dx.doi.org/10.1130/0016-7606(1990)102<0439.
WoldeGabriel, G., Walter, R.C., Aronson, J.L., Hart, W.K., 1992. Geochronology and distribution of silicic volcanic rocks of Plio-Pleistocene age from the central sector of the Main Ethiopian Rift. Quat. Int. 13-14:69–76. http://dx.doi.org/10.1016/1040-6182(92)90011-P.
WoldeGabriel, G., Heiken, G., White, T.D., Asfaw, B., Hart, W.K., Renne, P.R., 2000. Volcanism, tectonism, sedimentation, and the paleoanthropological record in the Ethiopian Rift System. Volcanic Hazards and Disasters in Human Antiquity:pp. 83–99 http://dx.doi.org/10.1130/0-8137-2345-0.83.
WoldeGabriel, G., Hart, W.K., Heiken, G., 2005. Innovative tephra studies in the East African Rift System. EOS Trans. Am. Geophys. Union 86:255. http://dx.doi.org/10.1029/2005EO270003.
Yimer, M., 1984. The petrogenesis, chemistry and hydrothermal mineralogy of rocks in the Langano-Aluto geothemal system, Ethiopia, Diploma report, Geothermal Institute, University of Auckland. Geothermal Institute, University of Auckland, New Zealand (75 pp.).